International Journal of Heat and Mass Transfer 217 (2023) 124687

Contents lists available at ScienceDirect

International Journal of Heat and Mass Transfer

journal homepage: www.elsevier.com/locate/ijhmt

Heat transfer and turbulent heat flux budgets in cooling films

Muting Hao *, Luca di Mare

Oxford Thermofluids Institute, University of Oxford, Southwell Building, Osney Mead, Oxford, OX2 0ES, United Kingdom

ARTICLE INFO

Keywords:
Film cooling
Turbulent heat flux
Transport equation
Self-similarity
Gas turbines
Large eddy simulation
Turbulent heat flux budgets
Fan-shaped holes

ABSTRACT

Statistics from large-eddy-simulation (LES) of cooling films with different cooling holes are used to evaluate budgets in the transport equation of turbulent heat flux. The capability of LES has been assessed by comparing simulated results with experimental data, while the correctness of the procedure generating turbulent heat flux budgets has been examined on a turbulent boundary layer. The mechanism of heat transfer has been preliminarily studied throughout the three-dimensional flow field at different blowing ratios using a general outer scaling, to recognize specific regions with corresponding heat transfer patterns. A compressible version of budget terms in the transport equation of turbulent heat flux is then explored to show the thermal behavior of flow downstream from the cooling film holes. Characteristics of each budget term are presented in a defect scaling consistent with the scaling suitable for Reynolds stresses and Reynolds stress budgets. Furthermore, these budget terms are compared among an array of different cooling hole shapes combined with different blowing ratios to explore self-similarity. Results show that the dynamic balance of all budget terms is significantly influenced by the cooling hole shape, while each turbulent heat flux budget term may scale with the velocity defect, temperature deficit, and the normalized streamwise distance to the power of an exponent dependent on the hole shape.

1. Introduction

The high-fidelity of prediction for film cooling has been pursued in recent years when higher and higher operating temperatures are being achieved in hot gas turbine components. The interest arises from the complexity of finding the optimal flow rate for the cooling stream. The thermodynamic cost of generating a cooling stream does not vary linearly with the flow rate due to the unsteady nature of three-dimensional film jets. Consequently, gaining a deeper insight into the flow and heat transfer mechanisms can greatly enhance film cooling designs.

While accurate prediction of film cooling flows can be achieved through advanced simulation methods such as Large Eddy Simulation (LES) and Direct Numerical Simulation (DNS), which offer increasing precision, designers often prefer Reynolds-averaged Navier-Stokes (RANS) methods due to their lower computational cost. However, the accuracy of RANS in predicting film cooling performance is limited by its turbulence models, which introduce inaccuracies in both Reynolds stresses and turbulent heat fluxes. For instance, [4] demonstrated RANS results with minimal lateral coolant spread and enhanced penetration downstream in the streamwise slices. Comparing these results with LES, they observed RANS overpredicting the turbulent heat flux, with values twice that of LES, resulting in an overprediction of the adiabatic cooling effectiveness of up to 45% on the centerline.

In the early stages, turbulent heat fluxes in the compressible version of transport equations were modeled using the strong Reynolds analogy, see Morkovin [17], drawing an analogy between turbulent momentum and heat transport. This approach, known as the strong Reynolds analogy, was established by Ribault and Friedrich [21]. The simplest subset of this method involved employing the Boussinesq hypothesis and assuming constant turbulent Prandtl numbers. However, this analogy is not applicable in complex flows, such as those with varying pressure gradients or interactions between shocks and turbulent boundary layers, as the turbulent Prandtl numbers cannot be predefined in such cases [21]. The limitations of the strong Reynolds analogy are also evident in film cooling flows. To achieve accurate predictions of turbulent heat fluxes, it is necessary to solve or model the transport equation of turbulent heat fluxes. Consequently, studying the budgets within these transport equations of turbulent heat fluxes becomes essential for improving the fidelity of predictions in such flows considering the following reasons.

First, detailed budgets in the transport equation of turbulent heat flux play a crucial role in advancing current turbulent heat flux models. Research has been conducted to model turbulent heat flux for

* Corresponding author.
E-mail address: muting.hao@eng.ox.ac.uk (M. Hao).

https://doi.org/10.1016/j.ijheatmasstransfer.2023.124687
Received 16 April 2023; Received in revised form 2 August 2023; Accepted 5 September 2023
Available online 20 September 2023

Nomenclature

Symbols

$< T''T'' >$	Favre-averaged temperature variance scaled by the temperature deficit, $< T''T'' >= \widetilde{T''T''}/\Delta T\Delta T$
$< T >$	Favre-averaged temperature scaled by the temperature deficit, $< T >= \widetilde{T}/\Delta T$
$< u''T'' >$	Favre-averaged streamwise turbulent heat flux scaled by the temperature deficit and velocity defect, $< u''T'' >= \widetilde{u''T''}/\Delta U\Delta T$
$< v''T'' >$	Favre-averaged wall-normal turbulent heat flux scaled by the temperature deficit and velocity defect, $< v''T'' >= \widetilde{v''T''}/\Delta U\Delta T$
β	Exponent factor
δ_{ij}	Kronecker delta
ϵ	turbulent viscous-thermal dissipation
$\widetilde{\Phi_{Ti}}$	Pressure-scrambling
$\widetilde{T''T''}$	Temperature variance
C_{Ti}	compressibility associated terms
D_{Ti}	turbulent viscous-thermal transport contribution
E	Total energy
k_T	Heat conduction coefficient
M_δ	Mach number in the scaling form
p	Pressure
Pr_δ	Prandtl number in the scaling form
q_i	Heat flux
Re_δ	Reynolds number in the scaling form
S_{kl}	Strain-rate tensor
T''	Turbulent temperature fluctuation
t	Time
$\bar{u}_c^+$	A van Driest transformation
ΔU	Streamwise velocity defect at $\delta_{99}/2$
δ_{99}	Boundary layer thickness, 99% far-field velocity point
δ_{v^*}	a semi-local viscous length
μ	viscosity
ρ'	Density fluctuation
ρ	Density
ρ_w	Near-wall density
σ_{ij}	Viscous stress tensor
$\sigma_{ij}^{(sgs)}$	Viscous stress tensor in the sub-grid scale
τ_w	wall shear stress
$\widetilde{T}$	Favre-averaged temperature
$\widetilde{u''T''}$	Turbulent heat flux in the streamwise direction
$\widetilde{u}_{MI}^+$	a Mach-invariant scaling
$\widetilde{v''T''}$	Turbulent heat flux in the wall-normal direction
D	Cooling hole diameter
f_{sgs}	The budget term of sub-grid scale effect in the transport equation of turbulent heat flux
M	Blowing ratio, $M = (\rho_c V_c)/(\rho_m V_m)$
Ma	Mach number
P_{Ti}^1	Production due to the mean velocity and mean temperature
P_{Ti}^2	Production due to the fluctuating strain rate
q_T	Turbulent heat flux vector
$q_T^{(sgs)}$	Turbulent heat flux vectorin the sub-grid scale
T''	Temperature fluctuation
T	Temperature
T_w	Wall temperature
T_{vd}^+	The temperature transformation
u''	Velocity fluctuation in the streamwise direction
U	Mean velocity in the streamwise direction
u_τ	friction velocity
v''	Velocity fluctuation in the wall-normal direction
V	Mean velocity in the wall-normal direction
V	Velocity
w''	Velocity fluctuation in the spanwise direction
W	Mean velocity in the spanwise direction
x	Streamwise distance from the center of the film-cooling hole
y	Coordinate in the Wall-normal direction
y^*	a wall-normal non-dimensional definition
y^+	Dimensionless wall distance
y_c^+	an integral length
z	Coordinate in the spanwise direction

Abbreviations

Con	Convection term
CT	Compressibility associated terms
DT	turbulent viscous-thermal transport contribution
eps	turbulent viscous-thermal dissipation
PHI	Pressure-scrambling
LES	Large eddy simulation
$PT1$	Production due to the mean velocity and mean temperature
$PT2$	Production due to the fluctuating strain rate
TKE	Turbulent kinetic energy

Subscript

c	coolant
m	mainstream

shear flows, with early work in the 1990s focusing on statistically two-dimensional compressible flows [21]. Comparisons between budgets of transport equations and modeled equations led to the proposal of improved turbulent heat flux models, surpassing the performance of algebraic models. Subsequently, in the 21st century, models were extended to three-dimensional situations. Bowersox [1] introduced an algebraic energy flux model (AEF) by truncating compressible turbulent heat flux transport equations, resulting in a 20% enhancement in temperature predictions over the traditional gradient diffusion model for moderately cooled turbulent boundary layers. The use of Bowersox's AEF model (see [1]) has been extended to higher Mach numbers, see Huang et al. [13], and to favorable pressure gradients, see Nicholson et al. [19,20].

Second, examining the budget terms in turbulent heat flux can provide insights into fluid physics. Nicholson et al. [19] conducted an assessment of existing modeling assumptions, demonstrating that the Boussinesq assumption yields accurate predictions of the Reynolds shear stress but compromises the accuracy of Reynolds normal stresses. Similarly, the constant turbulent Prandtl number model provides reasonable predictions for wall-normal turbulent heat flux but leads to inaccuracies in streamwise turbulent heat flux [19,4].

In the context of film cooling flows, investigating budget terms can offer valuable insights for developing higher-fidelity models, ultimately enhancing our understanding of flow mechanisms and optimizing cooling film designs. Despite its potential significance, there is currently no existing literature addressing this particular aspect to the best of the authors' knowledge. An earlier study by Muldoon and Acharya [18] examined budget terms of $k-\epsilon$ equations in cooling films using Direct Numerical Simulation (DNS). However, their analysis did not encompass the characteristics of turbulent heat flux, and they overlooked the influence of compressibility on their budget terms.

Furthermore, to effectively present the characteristics of turbulent heat flux and turbulent heat flux budgets, appropriate scaling methods are required. These methods are typically based on universal scal-

ing laws for turbulent velocity/turbulent temperature or mean velocity/mean temperature. In the context of compressible flows, an attempt has been made to identify a suitable scaling method among the different approaches associated with these universal scaling laws.

Considering the wall effect, the standard wall normalization is one such method, utilizing the scaled lengthscale $y+ = y/\delta_v$ and the scaled velocity $\bar{u}^+ = \bar{u}/u_\tau$. Here, the viscous lengthscale is $\delta_v = \nu_w/u_\tau$, where ν represents kinematic viscosity, and $u_\tau = \sqrt{\tau_w/\rho_w}$ is the friction velocity. However, the standard normalization does not perform optimally in the log-law region due to the assumption $\bar{\rho} = \rho_w$, which is not valid beyond the wall. An alternative is the van Driest density-weighted transformation, widely used in incompressible flows and adapted for compressible flows. This transformation yields good velocity profile collapses $u^+_{vd} = \int_0^{\bar{u}^+} \left(\bar{\rho}/\rho_w\right)^{1/2} d\bar{u}^+$ in cases where the compressibility effect is negligible. Other scaling methods have been proposed for specific flow configurations. Foysi et al. [6] employed y/h (where h is the half-channel height) in the outer scaling region of a supersonic channel flow with isothermal cooled walls. Huang et al. [14] introduced a semi-local viscous lengthscale $\delta_{v^*} = \bar{\mu}/\bar{\rho}u_{\tau^*}$ with a wall-normal non-dimensional definition $y^= y/\delta_{v^*}$ and a semi-local friction velocity $u_{\tau^*} = \sqrt{\tau_w/\bar{\rho}}$, yielding better collapses for local properties rather than wall properties in an isothermal compressible channel flow. Brun et al. [2] proposed an integral lengthscale $y^+_c = \int_0^{y^+} \left(\frac{\mu_w}{\mu}\right) dy^+$, accounting for strong near-wall temperature gradients. They also devised a van Driest transformation $\bar{u}^+_c = \int_0^{\bar{u}^+} \left(\frac{y^+}{y^{c+}}\right)\left(\frac{\mu_w}{\bar{\mu}}\right)\sqrt{\frac{\bar{\rho}}{\rho_w}} d\bar{u}^+$ to consider the effect of density and viscosity near the wall. This method demonstrated the ability to achieve collapses in the viscous sub-layer of isothermal cooled channels across a wide range of Mach numbers. Zhang et al. [29] developed a Mach-invariant scaling $\widetilde{u}^+_{MI} = \int_0^{\widetilde{u}^+} g\left(\frac{\mu_w}{\bar{\mu}}\right) d\widetilde{u}^+$ for compressible turbulent boundary layers using a viscosity-weighted transformation. Their scaling method was validated on compressible turbulent boundary layers with Mach numbers below 6 under the adiabatic wall condition.

Shadloo et al. [23] introduced a temperature transformation $T^+_{vd} = \int_0^{\bar{T}^+_t} \left(T_w/\bar{T}\right)^{1/2} d\bar{T}t^+$, which involves integrating the total temperature distribution across the boundary layer to resemble the van Driest velocity profiles $uvd^+ = \int_0^{\bar{u}^+} \left(\bar{\rho}/\rho_w\right)^{1/2} d\bar{u}^+$. This approach demonstrated good agreement between mean velocity profiles and incompressible DNS data from Schlatter et al. [22] in both the sub-layer and log-law regions for cases with adiabatic and heating walls.

However, when applied to cooling isothermal wall boundary layers, both the mean velocity profile and the total temperature profile exhibited deviations, similar to the findings of Duan and Martín [3]. Shadloo et al. [23] also revealed that the semi-local length scaling offers improved alignment of peaks in the Turbulent Kinetic Energy (TKE) budgets when comparing turbulent boundary layers with different heated walls. Nevertheless, this scaling method could not achieve a complete collapse of TKE budget terms. Also, Nicholson et al. [20] presented that the semi-local scaling is ineffective in collapsing Reynolds stress and TKE budget terms for hypersonic turbulent boundary layers with zero pressure gradient or favorable pressure gradients. As a result, Morkovin [17]'s hypothesis does not hold in such cases. This necessitates the development of new scaling methods to achieve collapsed Reynolds stress and heat flux statistics.

Furthermore, while there have been studies examining heat transfer characteristics in turbulent boundary layers (see [28,20,24,23]), channels (see [5]), and applications with practical significance ([15], [16]), the majority of these investigations have focused solely on near-wall flows. The scaling methods devised for studying heat transfer characteristics in these cases are primarily based on the near-wall region. In the context of film cooling, Hao and di Mare [10] mentioned that the main statistics downstream from the wall exhibit a two-layer structure, consisting of a layer close to the turbulent boundary layer in the near-wall region, and a layer in the jet region further away from the wall. For the scaling of the structure in the near-wall region, experience from existing scaling methods used in turbulent boundary layer studies can be leveraged. However, defining the outer scaling to be used across a range of blowing ratios in film cooling remains an open area of investigation when considering heat transfer downstream from the cooling film.

The primary aim of this research is to assess the budget terms in the compressible version of transport equations of turbulent heat flux for film cooling cases, utilizing the database provided by Hao and di Mare [10] based on Large Eddy Simulation (LES) data. The analysis focuses on two types of cooling holes: fan-shaped and cylindrical, with blowing ratios of 0.5, 1.0, and 1.5. The key emphasis lies in investigating the heat transfer characteristics downstream from the exit of the film cooling hole, specifically in the jet region (away from the wall), through the turbulence statistics of the flow. A crucial aspect of this study involves discussing the budgets of turbulent heat fluxes using a proposed scaling approach that facilitates the collapse of budget terms from various streamwise positions onto single curves. The overall objective is to shed light on the transport mechanisms underlying heat transfer in film cooling flows.

The following sections are structured as follows: Section 2 introduces the flow configuration, numerical scheme, budget equations of turbulent heat flux, and governing equations. Section 3 validates the approach using a turbulent boundary layer to demonstrate the budgets of turbulent heat flux. Section 4 presents the results of the study, encompassing an initial analysis of heat transfer in terms of mean temperature, temperature fluctuation, velocity fluctuation, density fluctuation, turbulent heat flux, and temperature variance in cooling films. This section then discusses the balancing of turbulent heat flux budgets in film cooling and its connection to the observed heat transfer mechanisms from the initial analysis. Finally, the universal scaling for each budget term is presented.

Overall, this paper offers valuable insights into the transport mechanisms of heat transfer in film cooling flows, which can be beneficial for designing more efficient cooling systems in practical applications.

2. Methodology

2.1. Flow configuration

The flow configuration, including the cooling film geometries, computational domain, and flow conditions, is intentionally selected to align with the cooling film experiment detailed in Gritsch et al.'s research paper (see [7]). Computational simulations are performed and validated by comparing the results with the experimental data from Gritsch et al. [7], as presented in Hao and di Mare [10].

In this study, two types of cooling holes are analyzed: the fan-shaped hole and the cylindrical hole. The geometries of these two film cooling holes are shown in Fig. 1. The fan-shaped hole has an inclination angle of 30 degrees and a length-to-diameter ratio of 6, with a hole diameter of 0.01 m. The lateral expansion angle for the fan-shaped hole is 14 degrees. The coordinate system employed to describe the hole positions is also depicted in Fig. 1, with the origin located at the center of the hole's exit plane. The x-axis corresponds to the direction of the streamwise flow, the y-axis is perpendicular to the wall, and the z-axis is aligned in the spanwise direction. Fig. 2 illustrates the corresponding computational domains for each cooling hole, comprising a mainstream channel, a coolant channel, and the cooling hole. The figure also outlines the near-field and far-field regions: the former refers to the region where x/D is located between 1 and 5, while the latter pertains to the region where x/D exceeds 5.

The mesh for the cooling films is generated using a template-based multi-block hexahedral meshing technique employed by the mesh generator, as explained in Hao et al. [12]. Fig. 3 showcases the fan-shaped mesh on the median cutting plane, along with a view where both the region $z < 0$ and $y > 0$ are blanked out. The $y+$ value is below 2, in-

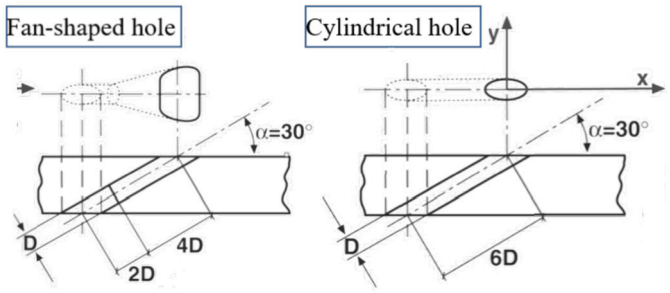

Fig. 1. The geometry of film cooling holes [7]: left (a) fan-shaped hole, right (b)cylindrical hole.

dicating an adequate mesh resolution. The quality of the mesh is also verified in Hao et al. [12].

The boundary conditions are set to match the specific operating conditions: the internal temperature $T_{tc} = 290K$, the temperature ratio $T_{tc}/T_{tm} = 0.54$, the internal Mach number $Ma_c = 0$, the external Mach number $Ma_m = 0.6$, the internal Reynolds number $Re_{Dc} \leq 2.5 \times 10^5$, the external Reynolds number $Re_{Dm} \leq 1.3 \times 10^5$, the boundary layer thickness $\delta_{99}/D = 0.5$, the external turbulence level $Tu_m/D \leq 1.5\%$, and the internal turbulence level $Tu_c/D \leq 1\%$. We focus on three blowing ratios for each type of cooling hole: $M = 0.5$, $M = 1.0$, and $M = 1.5$. An inflow generator proposed by Hao et al. [8] is applied to generate the inflow turbulence on the fly. For both external and internal channels, the outflow condition is the non-reflecting boundary condition, as described by Thompson [27]. The bottom wall of the external channel, the top wall of the internal channel, and the wall of the cooling hole are treated with the non-slip wall condition for velocity and the adiabatic wall condition for thermal behavior. The top wall of the external channel and the bottom wall of the internal channel are subject to the far-field boundary condition. The lateral boundaries in both channels are handled using the periodic boundary condition.

The simulations in this study are conducted using an in-house CFD code called 'H4X'. The Navier-Stokes equations are solved through an implicit LES approach using a finite volume method. Conservative variables are stored at the cell center, and inviscid fluxes are extrapolated at the cell interface using Roe's Riemann solver with gradients of characteristic variables obtained from a third-order compact scheme. This scheme eliminates oscillations near discontinuities and local extrema, achieving third-order accuracy away from these regions. Viscous fluxes, on the other hand, are reconstructed using least square gradients based on a four-point stencil, resulting in second-order accuracy. For time advancement, a third-order Runge-Kutta algorithm is employed, involving three evaluations of fluxes and four updates of conservative variables for each time step. The Courant-Friedrichs-Lewy (CFL) number is maintained below 0.8 to ensure numerical stability. The simulation is parallelized using MPI and OpenMPI, utilizing 480 processors for LES computations. Turbulent statistics are collected at the end of the simulations to account for initial transient solutions. A time series of statistics, covering at least 14 flow-through times, is sampled and subsequently post-processed into Favre-averaged quantities. For further details regarding numerical settings and the validity of LES results for film cooling cases analyzed in this study, refer to Hao and di Mare [10].

2.2. Budgets of turbulent heat flux

In compressible cases, dealing with turbulent heat flux modeling becomes more intricate compared to incompressible cases, as the momentum equation is no longer decoupled from the energy equation. The compressible transport equations of Reynolds fluxes are derived using mass conservation, the fluctuating momentum equation, and the fluctuating temperature equations. The gas is assumed to a perfect gas, and the buoyancy effect is assumed to be neglected.

The turbulent heat flux vector is denoted as $q_T = \overline{\rho u_i'' T''} = \bar{\rho}\widetilde{u_i'' T''}$, where $\widetilde{\ }$ represents the Favre averaging, and $\overline{\ }$ represents the Reynolds averaging. For a dependent variable f, the Reynolds decomposition splits f into an ensemble mean (the Reynolds average) and a fluctuation.

$$f(\mathbf{x}, t) = \bar{f}(\mathbf{x}, t) + f'(\mathbf{x}, t) \tag{1}$$

and the Favre decomposition partitions f into the Favre average and a fluctuation as

$$f(\mathbf{x}, t) = \tilde{f}(\mathbf{x}, t) + f''(\mathbf{x}, t) \tag{2}$$

where the Favre average is defined as

$$\tilde{f} = \frac{\overline{\rho f}}{\bar{\rho}} \tag{3}$$

The transport equation of the turbulent heat flux is

$$\begin{aligned} \frac{\mathrm{D}\bar{\rho}\widetilde{u_i'' T''}}{\mathrm{D}t} &= \frac{\partial\left(\bar{\rho}\widetilde{u_i'' T''}\right)}{\partial t} + \frac{\partial}{\partial x_k}\left(\widetilde{u}_k \bar{\rho}\widetilde{u_i'' T''}\right) \\ &= \bar{\rho} P_{Ti}^1 + \bar{\rho} P_{Ti}^2 + \bar{\rho}\Phi_{Ti} - \bar{\rho}\epsilon_{Ti} - \bar{\rho} D_{Ti} + \bar{\rho} C_{Ti} \end{aligned} \tag{4}$$

where the right-hand side is balanced among the production due to the mean velocity and mean temperature $\bar{\rho} P_{Ti}^1$, Production due to the fluctuating strain rate $\bar{\rho} P_{Ti}^2$, the 'Pressure-scrambling' term $\bar{\rho}\Phi_{Ti}$, the turbulent viscous-thermal dissipation term $\bar{\rho}\epsilon_{Ti}$, the turbulent viscous-thermal transport contribution $\bar{\rho} D_{Ti}$ and compressibility associated terms $\bar{\rho} C_{Ti}$. These terms are shown below:

(1) Production due to the mean velocity and mean temperature

$$\bar{\rho} P_{Ti}^1 = -\bar{\rho}\tau_{ik}\frac{\partial \widetilde{T}}{\partial x_k} - \bar{\rho}\widetilde{u_k'' T''}\frac{\partial \bar{u}_i}{\partial x_k} - \bar{\rho}(\gamma - 1)\widetilde{u_i'' T''}\widetilde{S}_{kk} + \left(\frac{\gamma}{c_p}\right)\overline{u_i'' \sigma_{jk}'}\widetilde{S}_{kj} \tag{5}$$

(2) Production due to the fluctuating strain rate

$$\bar{\rho} P_{Ti}^2 = \left(\frac{\gamma}{c_p}\right)\left[\overline{u_i'' \sigma_{jk}' s_{kj}''} - \overline{u_i'' p' s_{kk}''}\right] \tag{6}$$

(3) 'Pressure-scrambling'

$$\bar{\rho}\Phi_{Ti} = -\left[\overline{T''\frac{\partial p}{\partial x_i}}\right] \tag{7}$$

(4) Turbulent viscous-thermal dissipation

$$\begin{aligned} \bar{\rho}\epsilon_{T_i} &= -\left(\frac{\gamma}{c_p}\right)\overline{q_k'\frac{\partial u_i''}{\partial x_k}} + \overline{\sigma_{ik}'\frac{\partial T''}{\partial x_k}} \\ &= \left(\frac{\gamma}{c_p}\right)\left[\bar{k}_T\overline{\frac{\partial u_i''}{\partial x_k}\frac{\partial T'}{\partial x_k}} + k_T'\overline{\frac{\partial u_i''}{\partial x_k}\frac{\partial \bar{T}}{\partial x_k}} + \overline{k_T'\frac{\partial u_i''}{\partial x_k}\frac{\partial T'}{\partial x_k}}\right] + \left[\overline{\sigma_{ik}'\frac{\partial T''}{\partial x_k}}\right] \end{aligned} \tag{8}$$

(5) Turbulent viscous-thermal transport contribution

$$\begin{aligned} \bar{\rho} D_{Ti} &= -\left(\frac{\gamma}{c_p}\right)\frac{\partial}{\partial x_k}\left[\overline{u_i'' q_k'}\right] - \frac{\partial}{\partial x_k}\left[\overline{\rho u_i'' T'' u_k''} - \overline{\sigma_{ik}' T''}\right] \\ &= \left(\frac{\gamma}{c_p}\right)\frac{\partial}{\partial x_k}\left[\bar{k}_T\overline{u_i''\frac{\partial T'}{\partial x_k}} + \overline{k_T' u_i''}\frac{\partial \bar{T}}{\partial x_k} + \overline{k_T' u_i''\frac{\partial T'}{\partial x_k}}\right] \\ &\quad - \frac{\partial}{\partial x_k}\left[\overline{\rho u_i'' T'' u_k''} - \overline{\sigma_{ik}' T''}\right] \end{aligned} \tag{9}$$

(6) Compressibility associated terms

$$\bar{\rho} C_{Ti} = \overline{T''}\frac{\partial \bar{\sigma}_{ik}}{\partial x_k} + \left(\frac{\gamma}{c_p}\right)\left[\overline{u_i''\sigma_{jk}}\widetilde{S}_{kj} + \overline{u_i'' s_{kj}''}\left(\bar{\sigma}_{kj} - \bar{p}\delta_{kj}\right)\right] \tag{10}$$

2.3. Governing equations

In the governing equations, variables are non-dimensionalized by normalizing them with respect to the wall-normal distance at 99% of the far-field velocity δ_{99}, the velocity defect ΔU, and the temperature deficit ΔT. The resulting non-dimensional form of the governing equations is as follows:

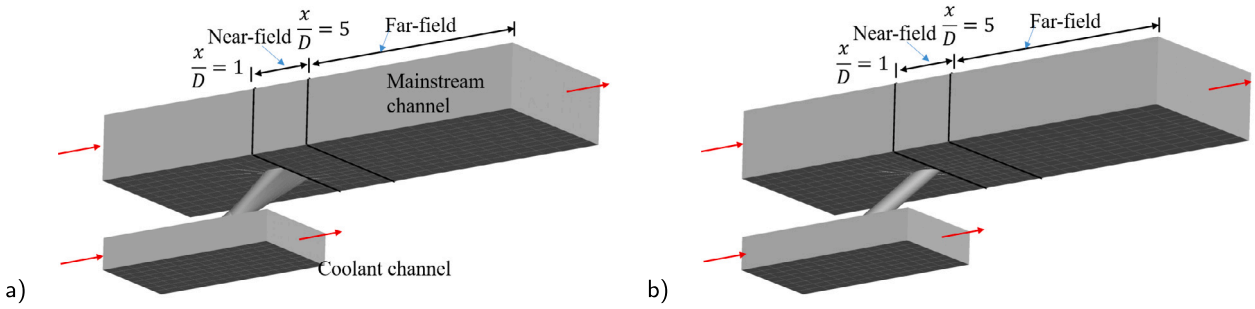

Fig. 2. Computational domains: a)fan-shaped hole, b) cylindrical hole.

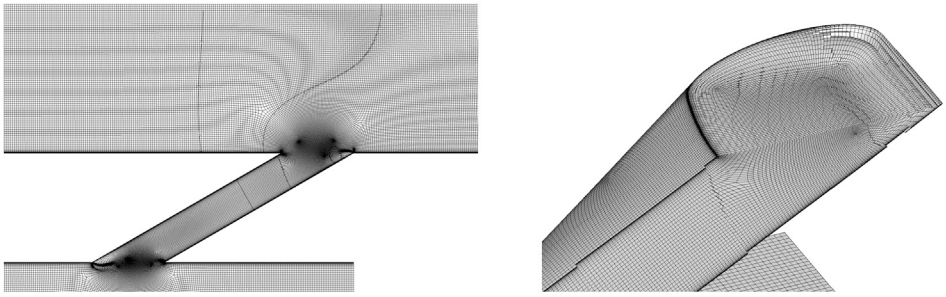

Fig. 3. The mesh of the fan-shaped case in the view on the median cutting plane and the view with both the median plane and the horizontal plane blanking.

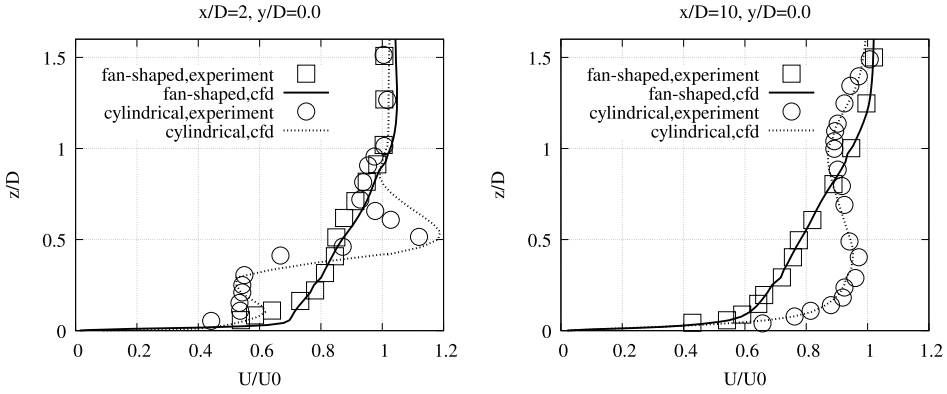

Fig. 4. Simulation results versus experimental results from Thole et al. [26].

$$\frac{\partial \rho}{\partial t}+\frac{\partial \rho u_j}{\partial x_j}=0$$

$$\frac{\partial \rho u_i}{\partial t}+\frac{\partial \rho u_i u_j}{\partial x_j}+\frac{\partial p}{\partial x_i}=\frac{1}{\partial x_j}\left(\partial \sigma_{ij}+\sigma_{ij}^{(sgs)}\right) \tag{11}$$

$$\frac{\partial \rho E}{\partial t}+\frac{\partial (\rho E+p)u_j}{\partial x_j}=\frac{1}{\partial x_j}\left(\partial \sigma_{ij}u_i-\partial q_j+\partial \sigma_{ij}^{(sgs)}u_i-\partial q_j^{(sgs)}\right)$$

where $u_i (i=1,2,3)$ is the velocity vector, with $(u_i,u_j,u_k)=(u,v,w)$. The directions of $i(i=1,2,3)$ correspond to (x,y,z), which are in the streamwise direction, wall-normal and spanwise direction. Other variables in Equ. (11) include the time t, the pressure p, the density ρ, the temperature T, the total energy $E=e+0.5u_iu_i$, the heat flux $q_i=-k_T\frac{\partial T}{\partial x_i}$, the viscous stress tensor σ_{ij} for a Newtonian fluid,

$$\sigma_{ij}=2\mu\left(S_{ij}-\frac{\delta_{ij}}{3}S_{kk}\right) \tag{12}$$

based on strain-rate tensor S_{kl}, which takes the form:

$$S_{kl}=\frac{1}{2}\left(\frac{\partial u_k}{\partial x_l}+\frac{\partial u_l}{\partial x_k}\right) \tag{13}$$

where μ is the viscosity and δ_{ij} is the Kronecker delta.

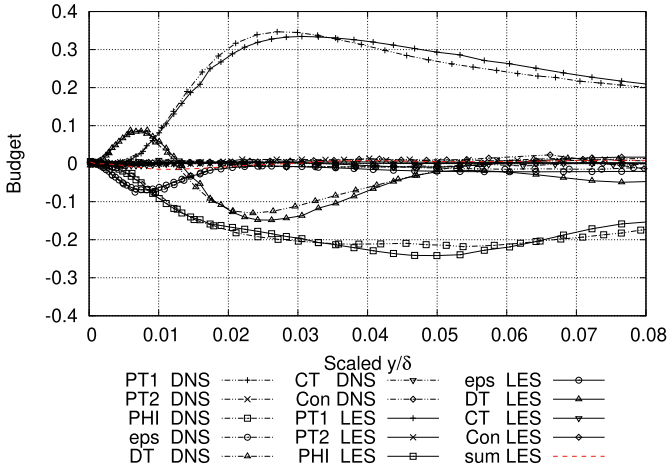

Fig. 5. Budget terms of $\widetilde{v''T''}$ for Spalart's turbulent boundary layer [25].

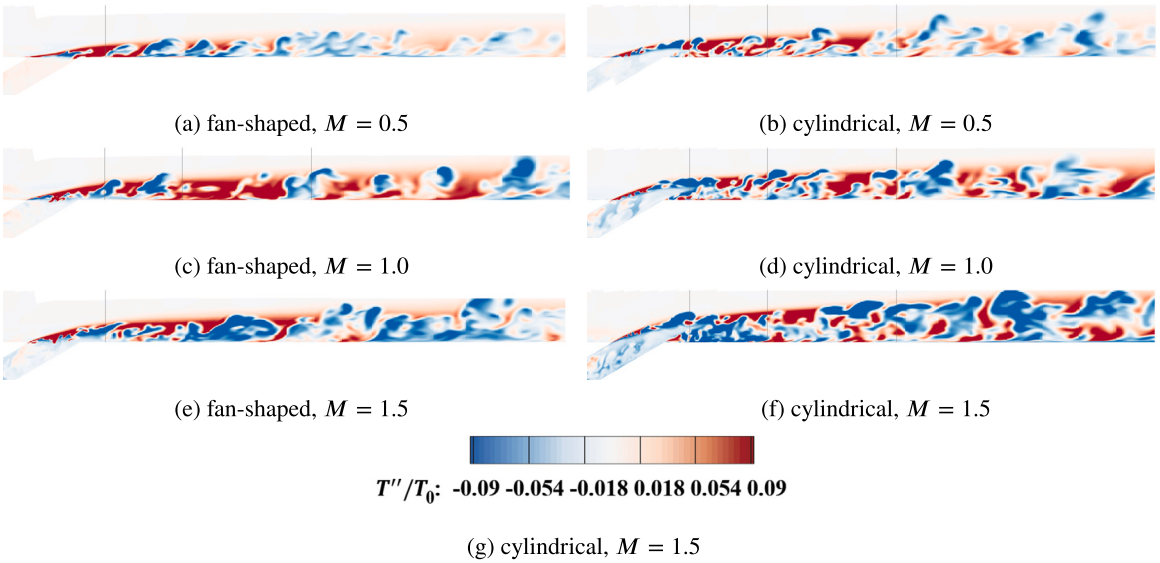

(a) fan-shaped, $M = 0.5$ (b) cylindrical, $M = 0.5$

(c) fan-shaped, $M = 1.0$ (d) cylindrical, $M = 1.0$

(e) fan-shaped, $M = 1.5$ (f) cylindrical, $M = 1.5$

(g) cylindrical, $M = 1.5$

Fig. 6. Contours of turbulent temperature fluctuation T'' scaled by T_0 on the median plane for fan-shaped and cylindrical films at $M = 0.5, 1.0, 1.5$. (For interpretation of the colors in the figure(s), the reader is referred to the web version of this article.)

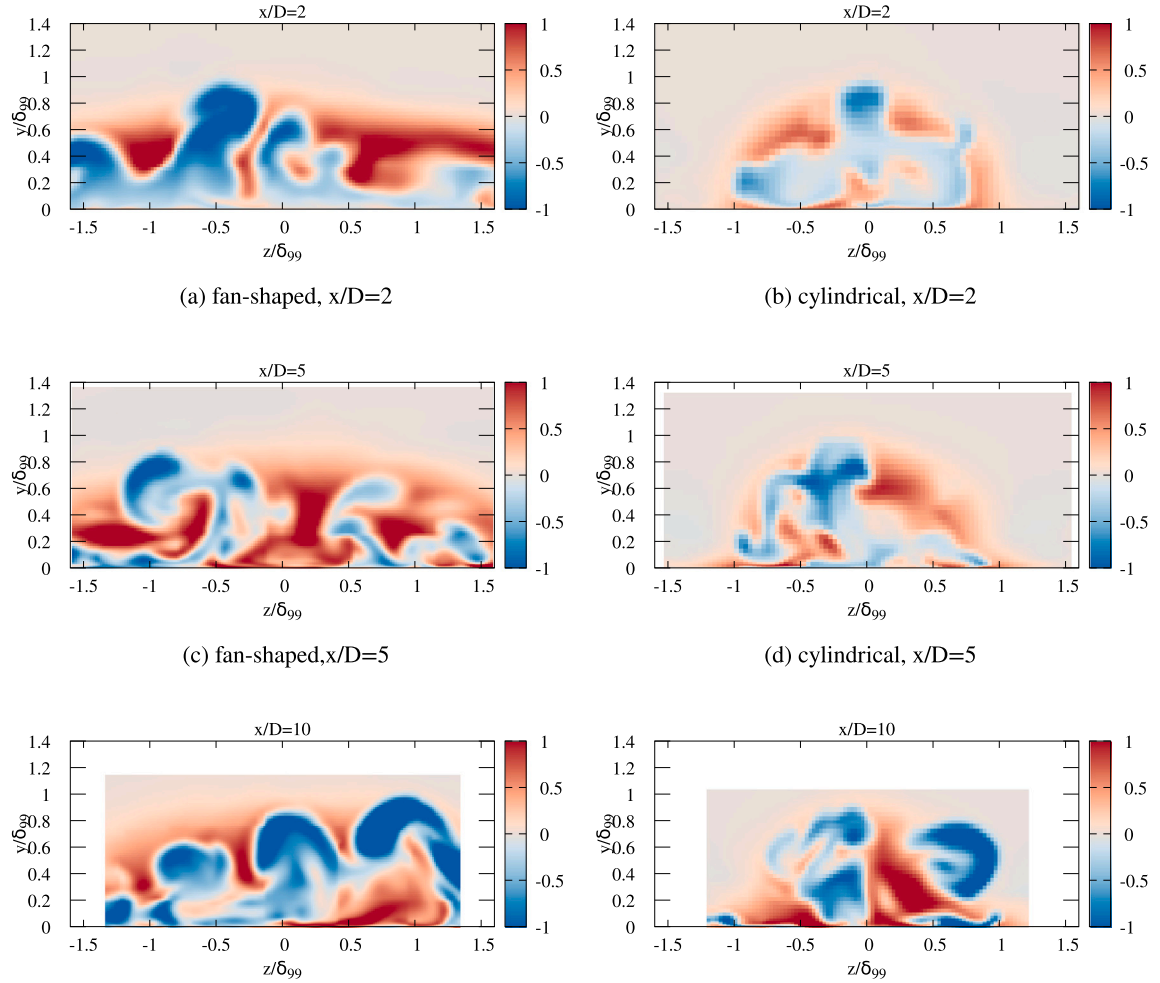

(a) fan-shaped, x/D=2 (b) cylindrical, x/D=2

(c) fan-shaped,x/D=5 (d) cylindrical, x/D=5

(e) fan-shaped, x/D=10 (f) cylindrical, x/D=10

Fig. 7. Contours of the turbulent temperature T'' scaled by ΔT for fan-shaped and cylindrical films at $M = 1.0$.

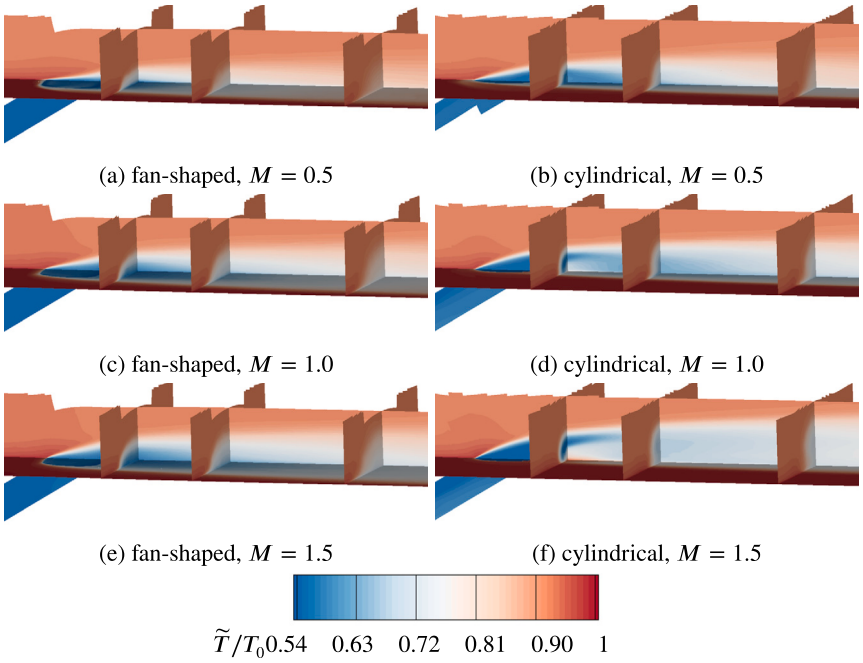

Fig. 8. Contours of Favre-averaged temperature $\widetilde{T}$ scaled by T_0 on the median plane for fan-shaped and cylindrical films at $M = 0.5, 1.0, 1.5$.

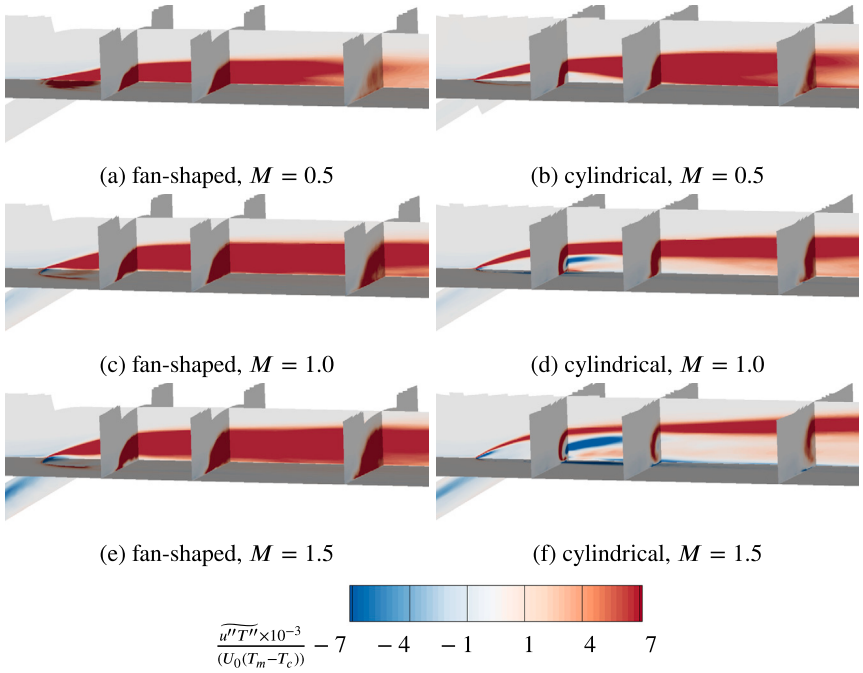

Fig. 9. Contours of turbulent heat flux in the streamwise direction $\widetilde{u''T''}$ scaled by $U_0(T_m - T_c)$ on the median plane for fan-shaped and cylindrical films at $M = 0.5, 1.0, 1.5$.

3. Validation

Two aspects of validation are conducted. The first part involves comparing the LES results of cooling films with experimental data to ensure the correctness of the simulations. Fig. 4 presents the velocity profile, which serves as a representative example of this validation. The agreement between the LES and experimental velocity profiles indicates that the numerical tool used in this study is capable of providing reasonably accurate budget results. Further validation, encompassing flowfield and heat transfer characteristics, is available in Hao and di Mare [10].

The second part of the validation process involves verifying the procedure for generating compressible turbulent heat flux budgets. To achieve this, a simulation of a turbulent boundary layer flow with an adiabatic wall is conducted using the LES code mentioned earlier. The computational domain dimensions are set as $100\delta^* \times 20\delta^* \times 25\delta^*$, where δ^* is the boundary layer displacement thickness. The grid spacing near the wall in the streamwise, wall-normal, and spanwise directions is set to $\Delta x^+ = 23$, $\Delta y^+ = 0.18$, and $\Delta z^+ = 7.8$ in wall units, respectively. The number of points in the wall-normal direction is adjusted to ensure 10 points within the 18 wall units of the wall. The total number of cells in the three dimensions is $256 \times 168 \times 192$. For this validation, the simu-

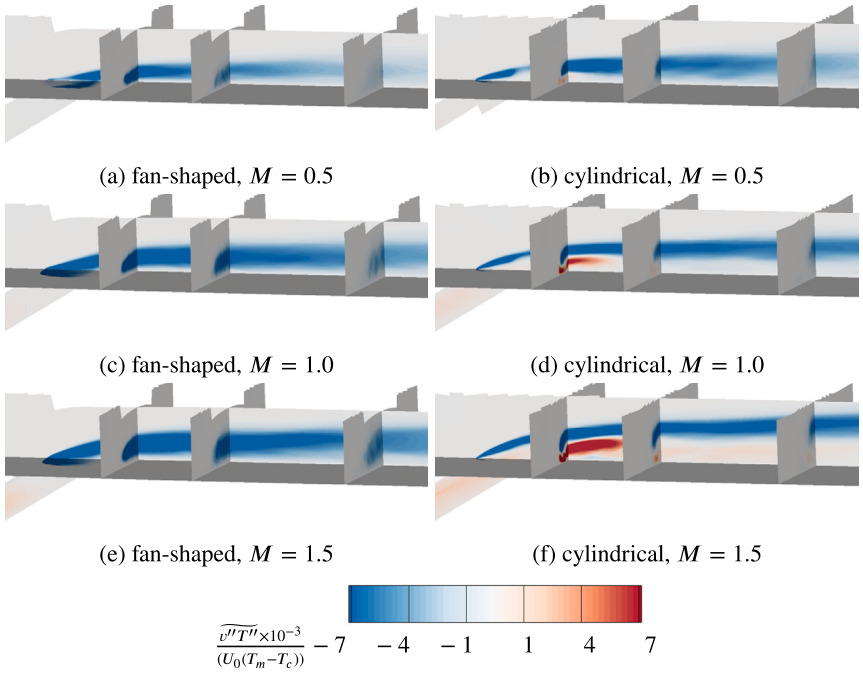

Fig. 10. Contours of the turbulent heat flux in the wall-normal direction $\widetilde{v''T''}$ scaled by $U_0(T_m - T_c)$ on the median plane for fan-shaped and cylindrical films at $M = 0.5, 1.0, 1.5$.

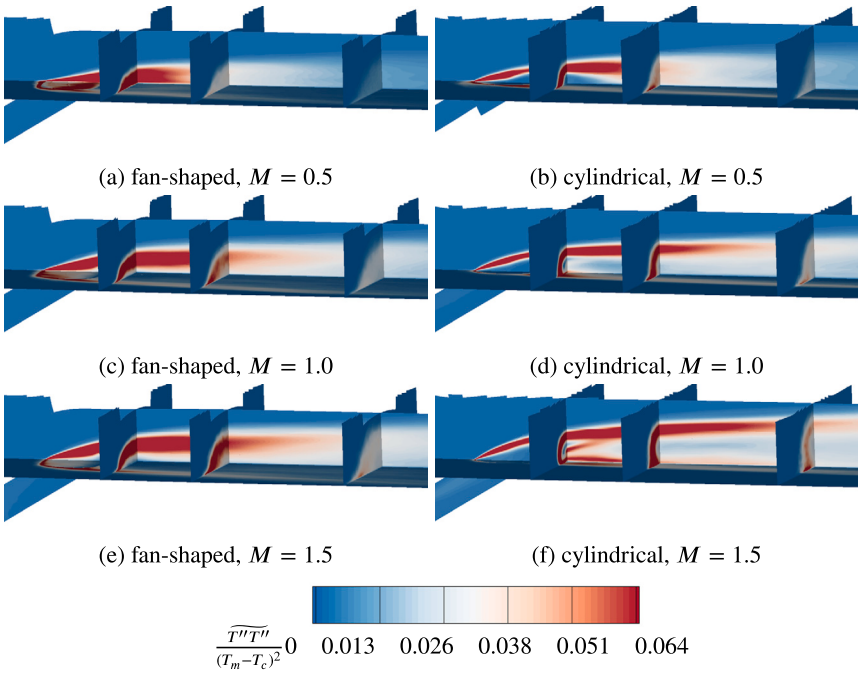

Fig. 11. Contours of the temperature variance $\widetilde{T''T''}$ scaled by $(T_m - T_c)^2$ on the median plane for fan-shaped and cylindrical films at $M = 0.5, 1.0, 1.5$.

lation is run for five flow-through times to ensure statistical steadiness of the turbulence, and then statistics are collected for ten flow-through times. The Favre-averages are obtained through a time average of 10 flow-through times on statistics, followed by spatial averaging within the mid strip of 60% of the spanwise dimension. The compressible turbulent heat flux budgets obtained from the LES results are compared with the DNS data from Shahab et al. [25], based on the given Mach number $M_\infty = 2.25$ and Reynolds number $Re_\infty = 25 \times 10^6$.

Fig. 5 displays the compressible turbulent heat flux budget terms in the wall-normal direction, using the LES result at the 60% streamwise dimension for comparison. Additionally, a sum of the imbalance and the loss of the sub-grid scale effect, as indicated in Equation (14), is shown (in red dash line) to indicate the aggregate error of the budget terms and the loss of unresolved dissipation. Equation (14) is derived by subtracting the left-hand side from the right-hand side of Equation (4), while assuming statistically stationary flow and ignoring the time-derivative term. The left-hand side sum includes the imbalance and the effect of sub-grid scales on the resolved budgets (represented by f_{sgs}).

$$Imbalance + f_{sgs} = \bar{\rho}P^1_{Ti} + \bar{\rho}P^2_{Ti} + \bar{\rho}\Phi_{Ti} - \bar{\rho}\varepsilon_{Ti} - \bar{\rho}D_{Ti} + \bar{\rho}C_{Ti} - \frac{\partial}{\partial x_k}\left(\widetilde{u}_k\bar{\rho}\widetilde{u''_i T''}\right) \tag{14}$$

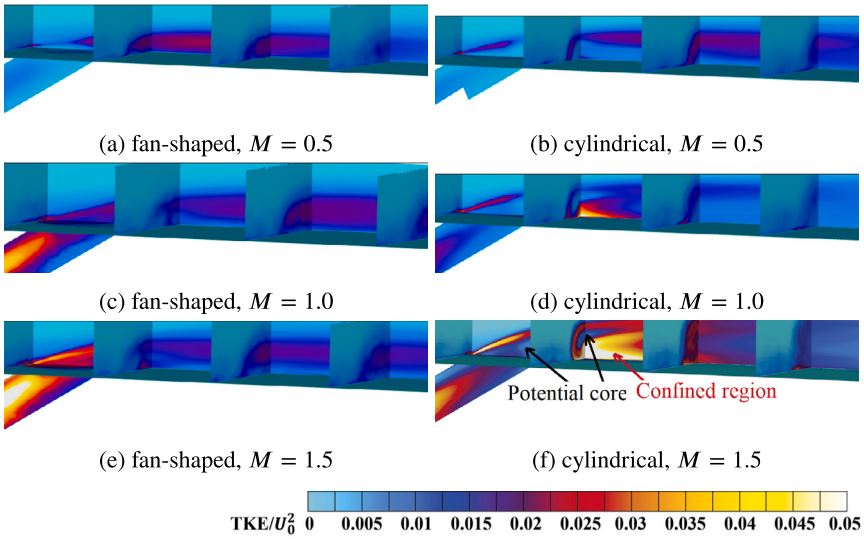

Fig. 12. Turbulence kinetic energy contours on the median plane for fan-shaped and cylindrical films at $M = 0.5, 1.0, 1.5$.

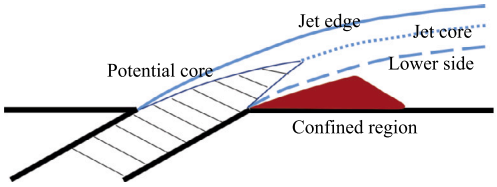

Fig. 13. A typical sketch of the confined region.

Table 1
Adjustment of regions in film cooling.

y/δ_{99}	$< T >$	$< u''T'' >$	$< v''T'' >$	$< T''T'' >$	Mechanism
0.6-0.8	+++	−	++	++	edge of jet
0.4-0.6	0	0	0	0	potential core
0.2-0.4	+	+	−	+	lower side of jet
0.0-0.2	++	0	0	0	confined region

* +: positive, ++: higher positive, +++: highest positive, −: negative.

The budgets derived from the current LES results exhibit good agreement with the DNS data in both the viscous layer and the log-law region. The maximum sum of the imbalance and unresolved dissipation occurs in the lower y^+ region, with a maximum deviation of 0.05. This indicates that the aggregate error of the budget terms is even smaller than the findings reported in the budget study by Vyas et al. [28].

Similarly, in the results shown in the next section, the imbalance and unresolved viscous terms are lumped together.

4. Results and discussion of film cooling

4.1. An initial analysis of heat transfer in film cooling

4.1.1. Fluctuations in the instantaneous flowfield

Fig. 6 presents the scaled turbulent temperature fluctuation T'' on the median plane for the cases described in Section 2. Grey lines are added at $x/D = 2, 5, 10$ to mark specific positions. The observed structures of hairpin vortexes near the wall downstream from the film indicate that these vortexes develop as the boundary layer thickness grows, which is influenced by the flow configuration. Using a scaling based on the local boundary layer thickness δ_{99} allows for a consistent comparison of flow field details based on the same dimension of the boundary layer.

By applying this method, Fig. 7 illustrates the contours of the scaled turbulent temperature fluctuation T'' on the $z-y$ planes at $x/D = 2, 5, 10$ for the two types of cooling films. Utilizing δ_{99} for the wall-normal distance scaling enables an easier comparison of coolant distribution and flow patterns within boundary layers across different flow configurations, as they are viewed within the same height of the boundary layer thickness. As seen from $x/D = 2$ to $x/D = 10$, the fan-shaped film exhibits varying numbers of flow structures occupying the space occupied by the coolant. For instance, Fig. 7e clearly shows three hairpin vortexes. On the other hand, in the cylindrical film, these structures are even more challenging to identify using other outer or inner scalings. Fig. 7b and Fig. 7d each provide evidence of a single hairpin vortex surrounding the coolant jet.

4.1.2. Favre-averaged flowfield

Fig. 8 - Fig. 11 present the Favre-averaged temperature $\widetilde{T}$ non-dimensionalized by T_0, the streamwise component of Favre-averaged turbulent heat flux $\widetilde{u''T''}$ non-dimensionalized by $U_0(T_m - T_c)$, the wall-normal component of Favre-averaged turbulent heat flux $\widetilde{v''T''}$ non-dimensionalized by $U_0(T_m - T_c)$, and the temperature variance $\widetilde{T''T''}$ non-dimensionalized by $(T_m - T_c)^2$ on the median planes together with $z-y$ slices at $x/D = 2, 5, 10$ of the film cooling cases studied. These contour plots provide a three-dimensional view of temperature and heat flux structures. The results indicate that in the fan-shaped films, the jet at different blowing ratios remains attached to the wall. Higher blowing ratios result in a thicker jet layer in the Cartesian streamwise, spanwise, and wall-normal directions (represented as (x, z, y) dimensions).

On the other hand, in the cylindrical film, Figs. 8 to 10 show that at $M = 0.5$, the jet detaches and reattaches to the wall after approximately $x/D = 5$. At $M = 1.0$, the jet detaches from the wall and maintains a roughly parallel flow after $x/D = 2$. At $M = 1.5$, the jet lifts off after $x/D = 2$. Additionally, Fig. 11 shows that in the cylindrical film, at $M = 1.0$ and $M = 1.5$, there is a triangular region on the median plane corresponding to low-temperature variance exiting from the cooling hole into the mainstream. This indicates the presence of a potential core, as supported by the turbulence kinetic energy shown in Fig. 12: the turbulence intensity generated inside the rear part of the cooing hole quickly decays to zero at the exit of the cooling hole when the jet comes into the mainstream. The potential core is clearly identified by both $\widetilde{T}$ (Fig. 8) and $\widetilde{T''T''}$ (Fig. 11). At $M = 1.0$ and $M = 1.5$, the potential core extends up to around $x/D = 3$ (Fig. 17), identifiable by an area of very low fluctuations in temperature and turbulent heat fluxes. In contrast, no recognizable potential core is observed in the fan-shaped film.

In addition, in the cylindrical film at $M = 1.0$ and $M = 1.5$, a confined region is observed just after the jet enters the mainstream, situated

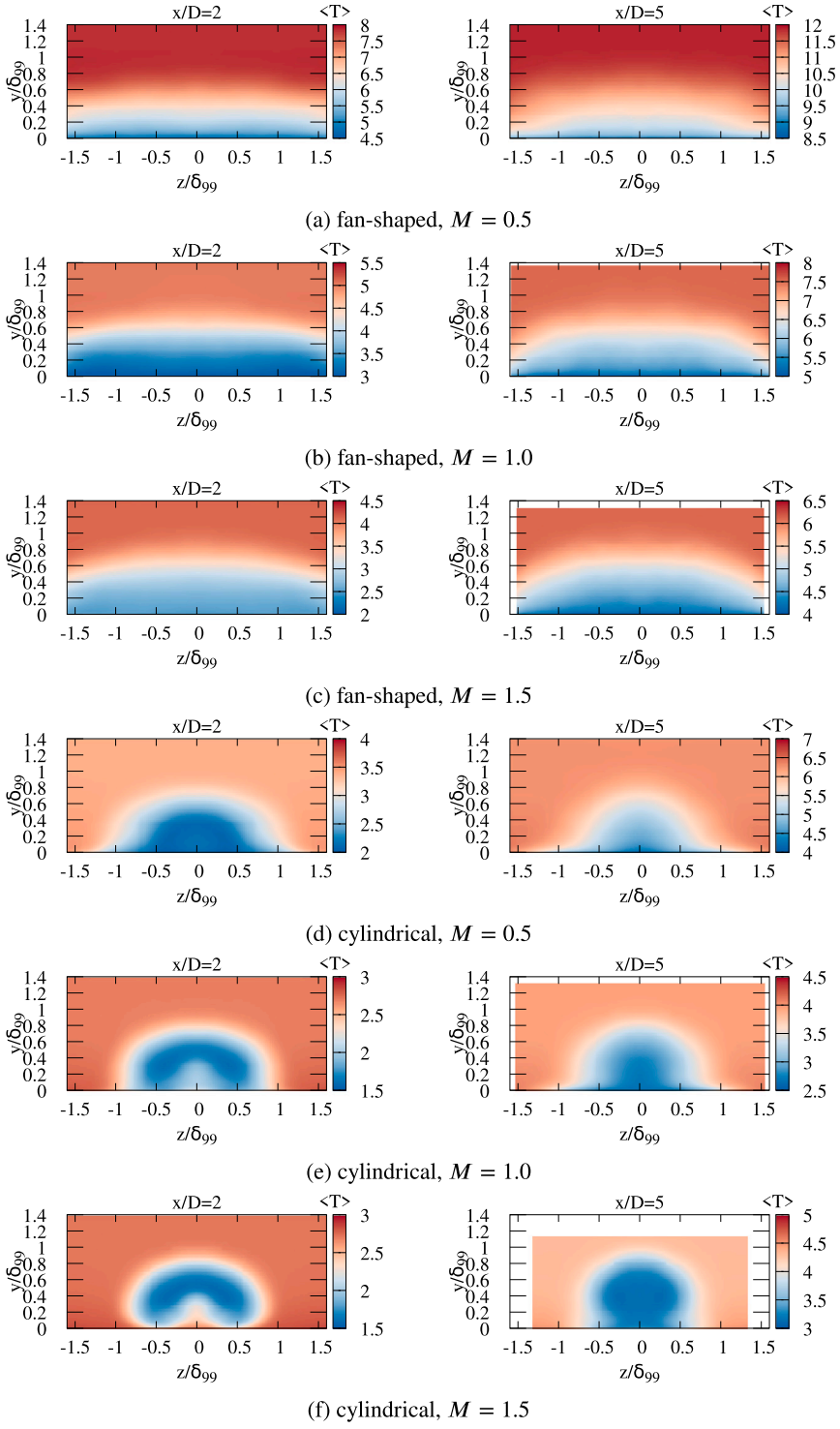

Fig. 14. Contours of the scaled Favre-averaged temperature $< T >$ on the median plane for fan-shaped and cylindrical films at $M = 0.5, 1.0, 1.5$.

below the lower side of the jet, under the potential core, and above the wall. This configuration can be seen at $x/D = 2$ in Fig. 8 and Fig. 11, and a sketch of a typical confined region is shown in Fig. 13. The confined region results from the confinement exerted by both the wall and the jet. Within this confined region, the flow and heat transfer are limited in the streamwise and wall-normal directions. Notably, at $M = 1.0$, the temperature $\widetilde{T}$ tends to be close to the minimum due to the jet's attachment to the wall, constraining the flow to remain within this region. Conversely, at $M = 1.5$, the temperature is higher as the hot stream is entrained. The turbulent heat flux components in the streamwise and wall-normal directions, $\widetilde{u''T''}$ and $\widetilde{v''T''}$, along with the temperature variance $\widetilde{T''T''}$, are generally weaker in the confined region compared to those observed in the surrounding jet. The confined region disappears around $x/D = 2$ at $M = 1.0$ and vanishes around $x/D = 5$ at $M = 1.5$.

The flow configurations exhibit similarities beyond $x/D = 10$, as also observed in Hao and di Mare [10]. Since the locations $x/D = 2, 5, 10$ represent crucial stages in the early development of the jet, the subsequent discussion will primarily focus on these locations.

Fig. 14 - Fig. 17 present the scaled quantities, including the Favre-averaged temperature $< T >$, the streamwise component of Favre-

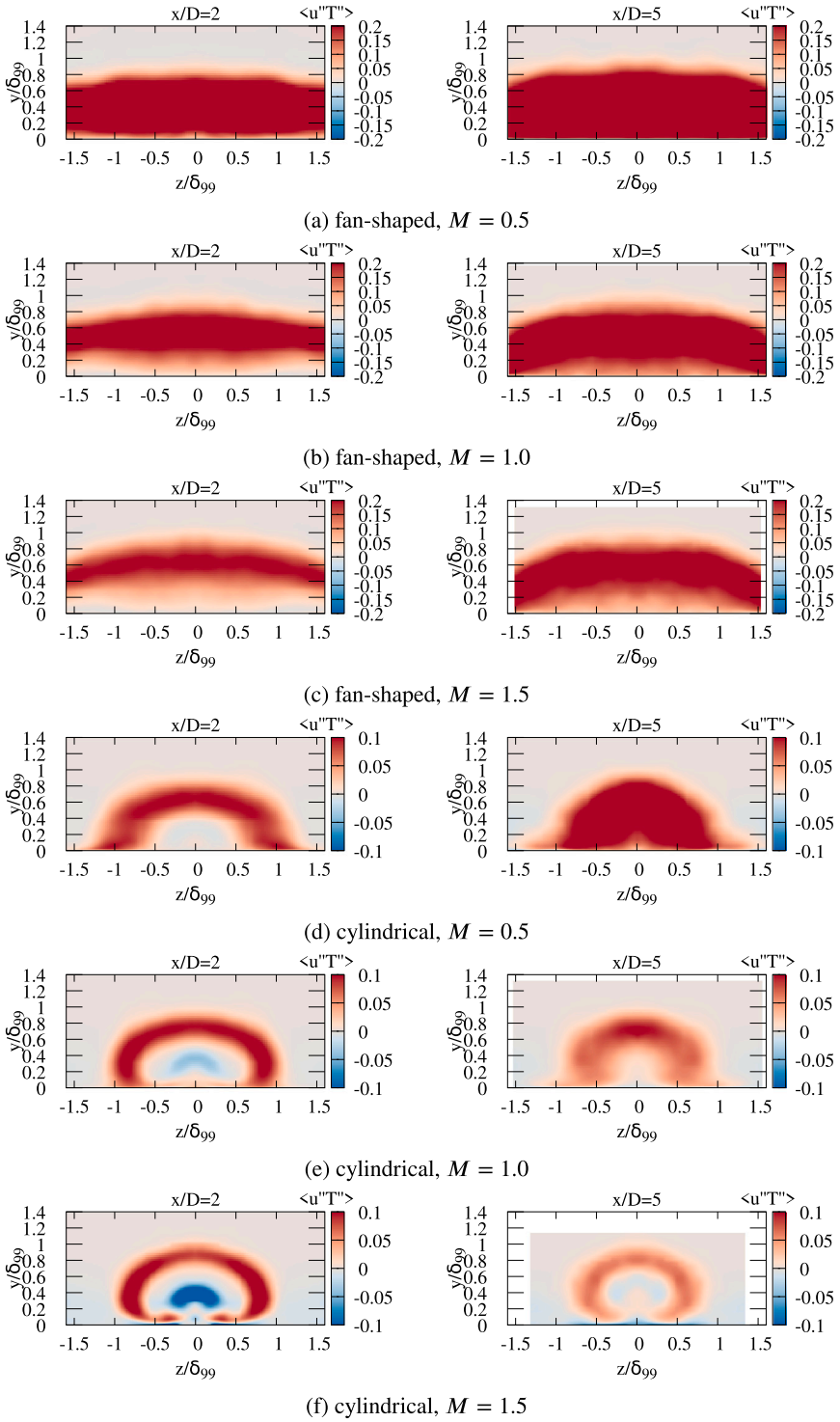

Fig. 15. Contours of the scaled turbulent heat flux in the streamwise direction $< u''T'' >$ on the median plane for fan-shaped and cylindrical films at $M = 0.5, 1.0, 1.5$.

averaged turbulent heat flux $< u''T'' >$, the wall-normal component of Favre-averaged turbulent heat flux $< v''T'' >$, and the temperature variance $< T''T'' >$ on $z-y$ slices at $x/D = 2, 5, 10$. The notation <> represents the scaled Favre-averaged quantity. Prior to scaling, these quantities are first Favre-averaged and then scaled according to the boundary layer thickness δ_{99}, velocity defect ΔU, and temperature deficit ΔT. Specifically,

$$< T >= \widetilde{T}/\Delta T \tag{15}$$

$$< u''T'' >= \widetilde{u''T''}/(\Delta U \Delta T) \tag{16}$$

$$< v''T'' >= \widetilde{v''T''}/(\Delta U \Delta T) \tag{17}$$

$$< T''T'' >= \widetilde{T''T''}/(\Delta T \Delta T) \tag{18}$$

For the fan-shaped cases, the Favre-averaged temperature (shown in 14a, 14b, 14c), the variance of temperature (shown in 17a, 17b, 17c), and turbulent heat fluxes (shown in 15a, 15b, 15c and 16a, 16b, 16c) are concentrated in a weakly curved layer around $y/\delta_{99} = 0.4 - 0.6$.

In the case of the cylindrical film, the blowing ratio determines the strength of the second motion in the $z-y$ plane, and this motion influences the configuration of the jet. At $M = 0.5$, the jet spreads across

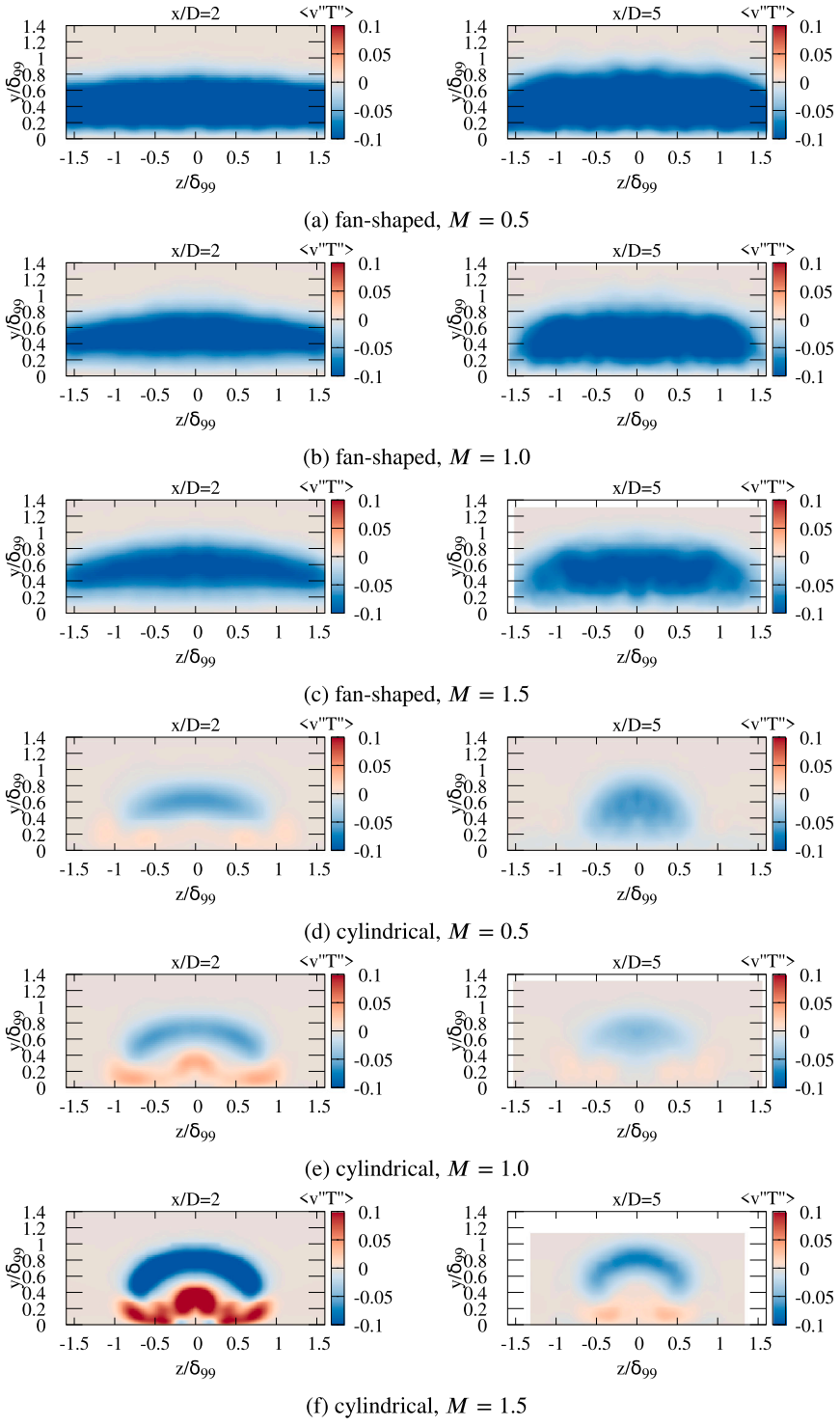

Fig. 16. Contours of the scaled turbulent heat flux in the wall-normal direction $< v''T'' >$ on the median plane for fan-shaped and cylindrical films at $M = 0.5, 1.0, 1.5$.

the range from $z/\delta_{99} = -1$ to 1 in the spanwise direction and below $y/\delta_{99} = 1$ in the wall-normal direction. At $M = 1.0$, the jet is confined within the range from $z/\delta_{99} = -1$ to 1 in the spanwise direction and below $y/\delta_{99} = 1$ in the wall-normal direction. At $M = 1.5$, the jet is confined within the range from $z/\delta_{99} = -1$ to 1 in the spanwise direction and $y/\delta_{99} = 0.2 - 1$ in the wall-normal direction. Two specific regions are of interest:

1) The presence of a potential core can be recognized by observing low levels of temperature variance $< T''T'' >$. For instance, at $M = 1.0$ (as depicted in Fig. 17e), the potential core is generally located around $y/\delta_{99} = 0 - 0.6$, and around $y/\delta_{99} = 0.4 - 0.6$ on the centerline. Similarly, at $M = 1.5$ (shown in Fig. 17f), the potential core is found around $y/\delta_{99} = 0.2 - 0.6$ in general, and particularly around $y/\delta_{99} = 0.4 - 0.6$ on the centerline. This observation is also evident in Fig. 12f.

2) The confined region can be identified by observing low levels of the wall-normal component of the turbulent heat flux $< v''T'' >$, and it is located below approximately $y/\delta_{99} = 0.2$ at both $M = 1.0$ (shown in Fig. 16e) and $M = 1.5$ (shown in Fig. 16f). This observation is also evident in Fig. 12f.

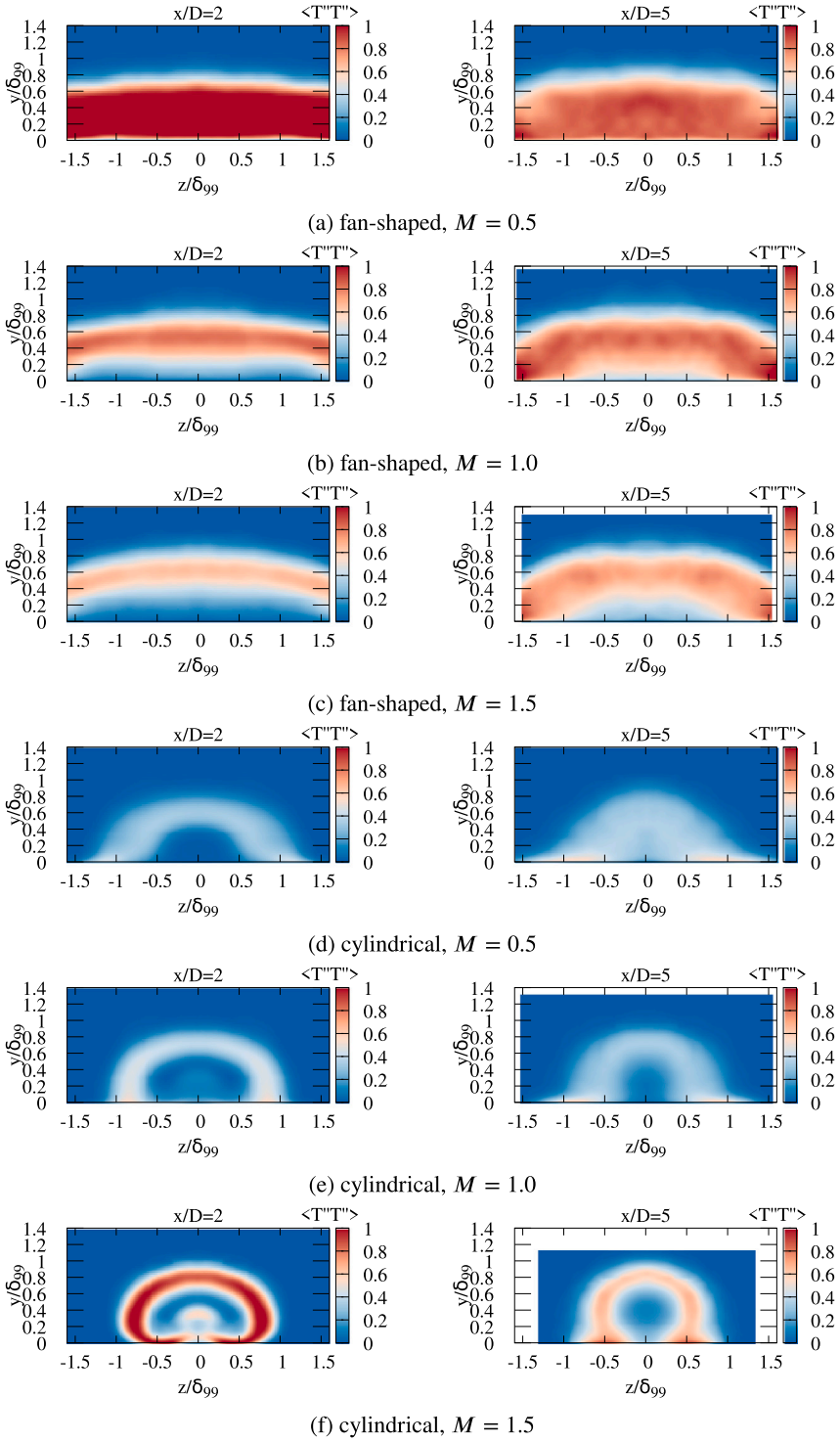

Fig. 17. Contours of the temperature variance $< T''T'' >$ on the median plane for fan-shaped and cylindrical films at $M = 0.5, 1.0, 1.5$.

Table 1 presents a judgment scheme for specific regions based on the Favre-averaged temperature $< T >$, temperature variance $< T''T'' >$, and turbulent heat fluxes $< u''T'' >$ and $< v''T'' >$. The symbols '-' and '+' indicate negative and positive values, respectively. Furthermore, '++' represents a higher positive value than '+', and '+++' represents an even higher positive value than '++'. '0' indicates a value close to the minimum absolute value of the corresponding quantity. In summary, Table 1 provides a way to identify different specific regions in the downstream flow from a cooling film. For instance, a positive value for $< T >$, $< T''T'' >$, and $< v''T'' >$ combined with a negative value for $< u''T'' >$ indicates the edge of the jet. Conversely, when all four quantities are close to their minimum, it signifies the potential core. Moreover, if $< T >$, $< T''T'' >$, and $< u''T'' >$ are positive while $< v''T'' >$ is negative, it identifies the lower side of the jet. Lastly, a high positive value for only $< T >$ with the other three quantities close to zero indicates the confined region.

4.2. The balancing of turbulent heat flux budgets in film cooling

To analyze the different budget terms in the transport equation of turbulent heat fluxes, following Equations (5) to (10), a defect scal-

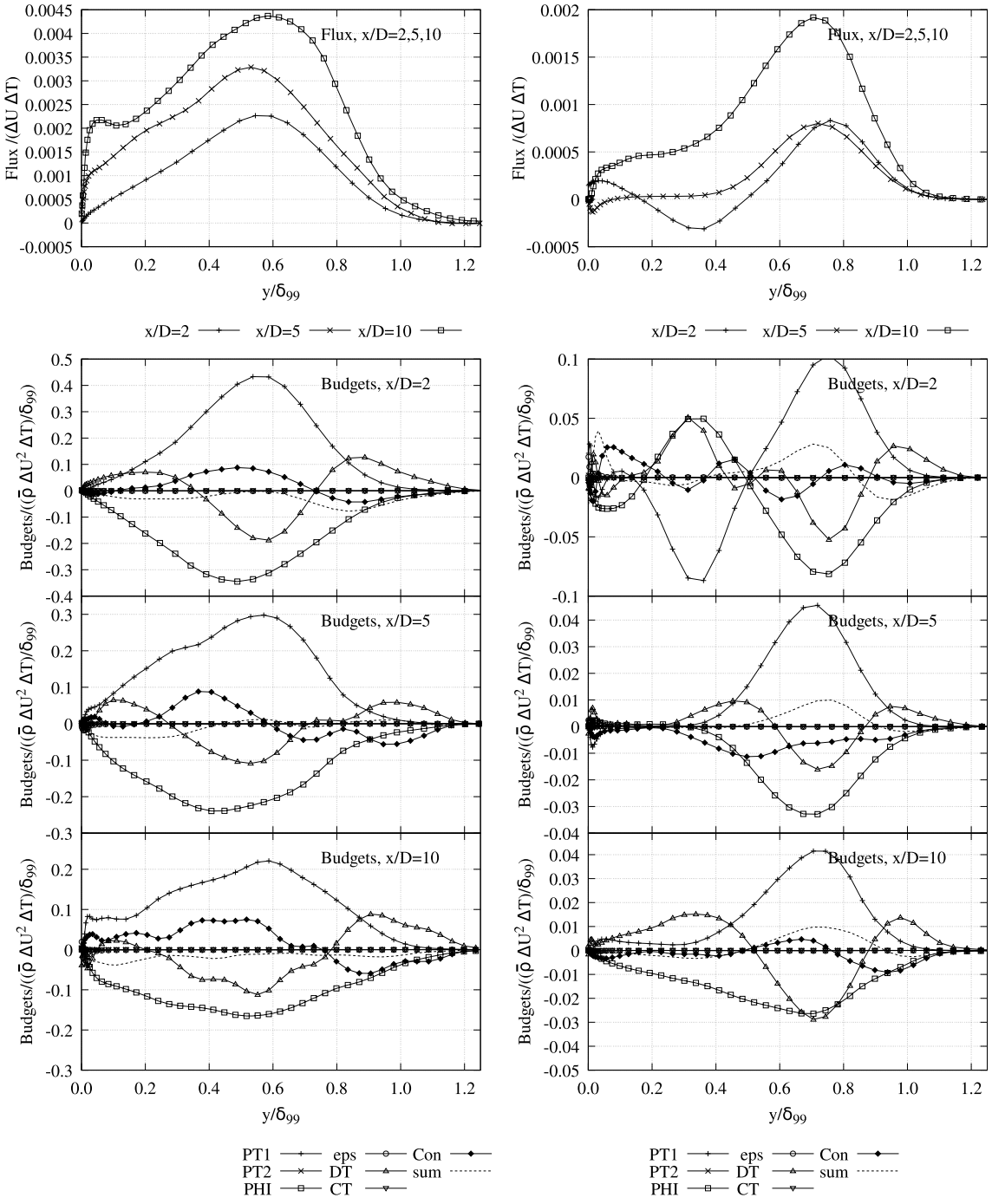

(a) fan-shaped hole (b) cylindrical

Fig. 18. Streamwise turbulent heat flux $\widetilde{u''T''}$ scaled by $\Delta U \Delta T$ and Budget terms of $\widetilde{u''T''}$ scaled by $\Delta U^2 \Delta T/\delta_{99}$ for fan-shaped and cylindrical films at $M = 1.0$.

ing method is employed. This involves normalizing the variables using the boundary layer thickness δ_{99}, velocity defect ΔU, and temperature deficit ΔT. Additionally, the turbulent heat fluxes $\widetilde{u''T''}$ and $\widetilde{v''T''}$ are scaled by $\Delta U \Delta T$, while the budget terms of $\widetilde{u''T''}$ and $\widetilde{u''T''}$ are scaled by $\Delta U^2 \Delta T/\delta_{99}$. Figs. 18 and 19 illustrate the scaled turbulent heat fluxes and the corresponding budget terms of the turbulent heat fluxes on the centerline for both fan-shaped and cylindrical films at a blowing ratio of $M = 1.0$. The statistics are averaged laterally across a narrow mid strip ranging from −0.15D to 0.15D.

In Fig. 18 (top row), the variations of the streamwise component of the turbulent heat flux correlations across the jet layer downstream from the cooling hole are shown with the defect scaling. Comparing Fig. 18 (top row) with Fig. 19 (top row), it is evident that the streamwise flux exceeds the wall-normal turbulent heat flux in both fan-shaped and cylindrical cooling films.

In the fan-shaped cases, there is an approximately 43% increase in the magnitude of the streamwise heat flux peak from $x/D = 2$ to $x/D = 5$, and at $x/D = 10$, the magnitude reaches 190% of its initial value, as shown in Fig. 18 (first row, left). The position of this peak corresponds

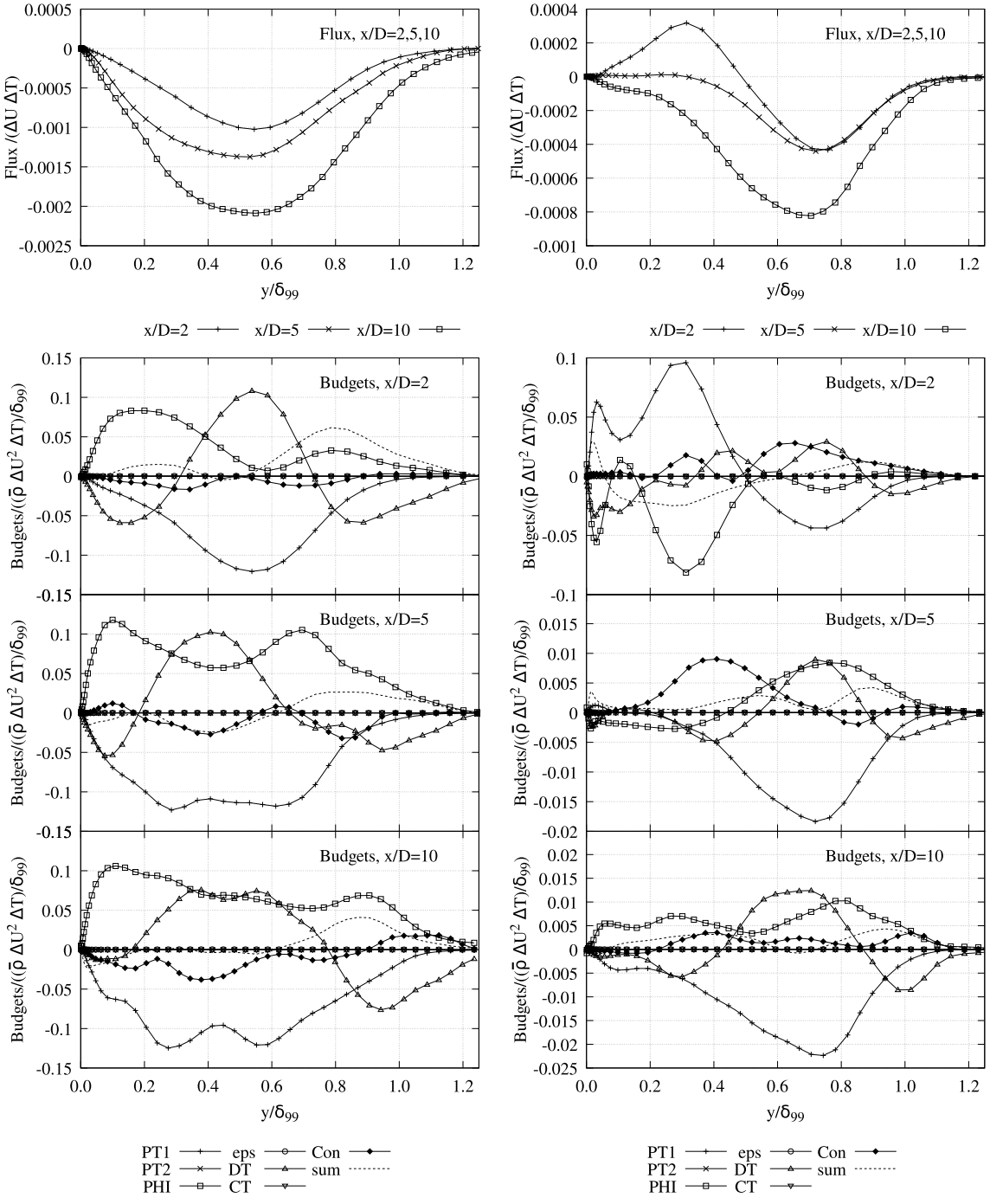

(a) fan-shaped hole (b) cylindrical

Fig. 19. Wall-normal turbulent heat flux $\widetilde{v''T''}$ scaled by $\Delta U \Delta T$ and multiple budget terms of $\widetilde{v''T''}$ scaled by $\Delta U^2 \Delta T/\delta_{99}$ for fan-shaped and cylindrical films at $M = 1.0$.

to the edge of the jet. The current defect scaling using δ_{99} preserves the position of this peak, while the outer scaling or semi-local scaling does not maintain its position. In contrast, for the cylindrical cooling film, as seen in Fig. 18 (first row, right), the streamwise heat flux shows no change from $x/D = 2$ to $x/D = 5$. However, from $x/D = 5$ to $x/D = 10$, the magnitude of the corresponding peak increases to more than twice its initial value due to the edge of the jet. The location of the peak magnitude for the cylindrical film is at around $y/\delta_{99} = 0.7 - 0.8$ with the defect scaling, indicating that the jet layer thickness is greater in the cylindrical film compared to the fan-shaped film. Notably, the heat flux resulting from mixing on the edge of the jet improves uniformly along the streamwise distance downstream from the hole in the fan-shaped film, whereas in the cylindrical film, the enhancement of heat flux due to jet edge mixing occurs only from the far field.

In addition to the peak present on the edge of the jet, the streamwise component of the heat flux in the cylindrical film presents another peak in the proximity of the wall when the jet just comes out from the hole at $x/D = 2$. Between these two peaks, there is a local minimum with a

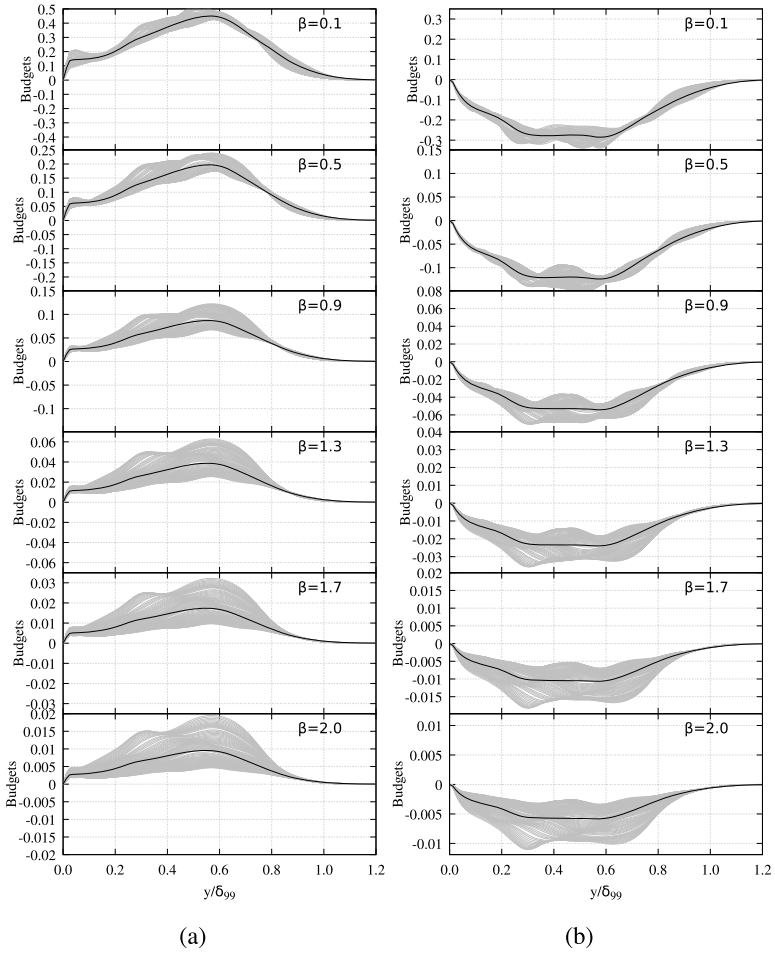

Fig. 20. The budget term (production due to the mean velocity and mean temperature $PT1$) of (a) $\widetilde{u''T''}$ scaled by $(\Delta U^2 \Delta T(x/D)^{-\beta}/\delta_{99}$, (b) $\widetilde{v''T''}$ scaled by $(\Delta U^2 \Delta T(x/D)^{-\beta}/\delta_{99}$ for fan-shaped film at the blowing ratio $M = 1.0$. Grey lines: multiple curves on streamwise positions between $x/D = 5$ and $x/D = 16$, Black lines: Master curve (Average of multiple gray curves). For each column from the top to bottom are the result using $\beta = 0.1, 0.5, 0.9, 1.3, 1.7, 2.0$.

negative flux value around $y/\delta_{99} = 0.35$, corresponding to the lower side of the jet. This region below $y/\delta_{99} = 0.35$ corresponds to the confined region described earlier in the previous section. It can be identified in the area of high temperature variance on the slice at $x/D = 2$ in Fig. 11. This confined region spans from above the wall to below the lower side of the potential core, which is located at around $y/\delta_{99} = 0.5$ where the turbulent heat flux is zero.

The heat flux dynamics can be analyzed by examining the budgets for the streamwise component $\widetilde{u''T''}$ and the wall-normal component $\widetilde{v''T''}$. Fig. 18 (rows 2 to 4, left column) presents the budget terms for the transport equation of the streamwise turbulent heat flux for the fan-shaped film at $M = 1.0$. At $x/D = 2$, within most of the thickness of the wall jet, the main gain in the budgets of $\widetilde{u''T''}$ is attributed to the production due to the mean velocity and mean temperature ($PT1$). The main loss is due to pressure scrambling (Φ). The peak of these two terms is located around $y/\delta_{99} = 0.5$, which corresponds to the edge of the jet. The next term in magnitude is the turbulent viscous-thermal transport contribution (DT). This term transports the $\widetilde{u''T''}$ flux from the edge of the jet ($y/\delta_{99} = 0.5$) to above (approximately $y/\delta_{99} = 0.8$) and towards the wall. Convection acts as a gain at the edge of the jet and a loss above it. These budget terms represent net gain and loss for control volumes drawn around a narrow strip near the center plane. The net loss due to convection beyond the edge of the jet (y/δ_{99}) occurs because the streamwise convective flux of $\widetilde{u''T''}$ grows in the streamwise direction, and there is no contribution from the wall-normal velocity (V). The net gain due to convection occurs beyond the edge of the jet ($y/\delta_{99} = 0.5$) since high values of $\widetilde{u''T''}$ are convected downwards by the fact that V is negative throughout the entire thickness of the jet. At $x/D = 5$, most budget terms retain their shape, with the magnitude of each term slightly reduced. The relative size of each term is also preserved. Upon reaching $x/D = 10$, most budget terms maintain their shape, except for the region near the wall. In the near-wall region, the balance of $\widetilde{u''T''}$ budget terms starts to exhibit pattern typical of a turbulent boundary layer: the turbulent viscous-thermal transport contribution (eps) becomes a loss and rapidly diminishes towards the wall, while the production due to the mean velocity and mean temperature ($PT1$) becomes the primary gain throughout the jet layer's thickness. These two terms are counterbalanced by pressure scrambling as the loss. Throughout the inner layer considered in this study, the contribution of the production due to the fluctuating strain rate ($PT2$) is found to be negligible.

Fig. 18 (row 2-4, right column) illustrates the budget terms in the transport equation of the streamwise turbulent heat flux for the cylindrical film at $M = 1.0$. At $x/D = 2$, the budget terms of $\widetilde{u''T''}$ within the jet region between $y/\delta_{99} = 0.5$ and $y/\delta_{99} = 1.2$ of the cylindrical film exhibit similar shapes as the corresponding budget terms for the fan-shaped film throughout the entire jet layer thickness of the fan-shaped case. However, the magnitudes of these budget terms for the cylindrical film are approximately 20% of those for the fan-shaped film. This indicates that the structure of $\widetilde{u''T''}$ budget terms above the center of the potential core in the cylindrical film correspond to the structure of $\widetilde{u''T''}$ budget terms above the wall in the fan-shaped film. For the cylindrical film, between $y/\delta_{99} = 0.1$ and $y/\delta_{99} = 0.5$, the main budget terms reverse their signs compared to those in the region above the potential core. The production $PT1$ of $\widetilde{u''T''}$ becomes negative and acts as a

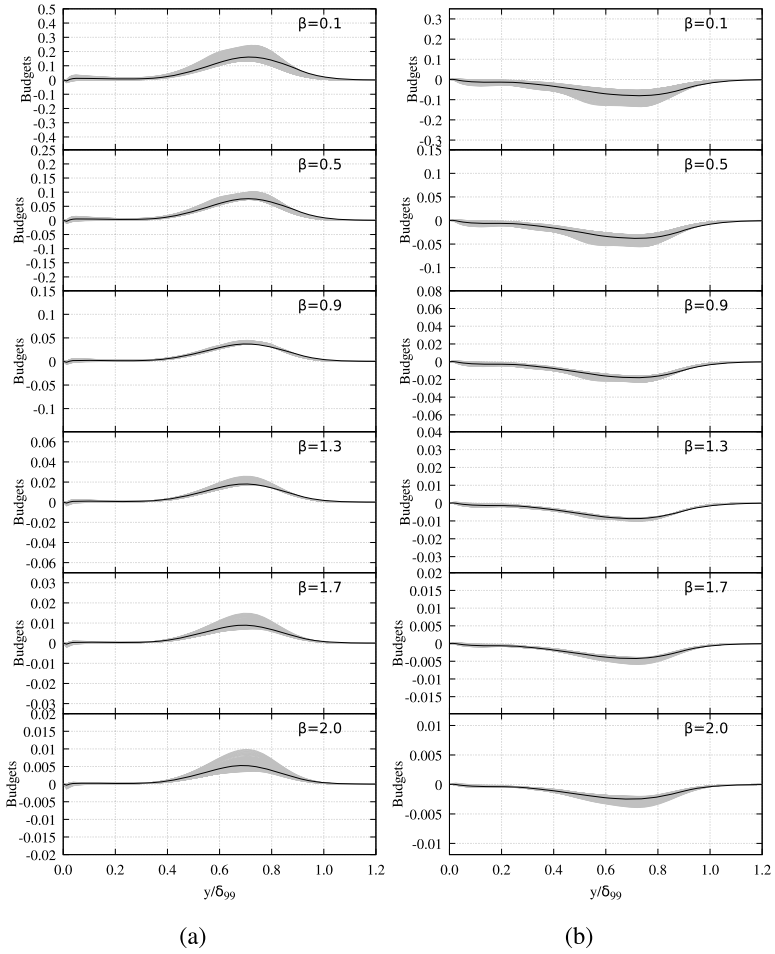

Fig. 21. The budget term (production due to the mean velocity and mean temperature $PT1$) of (a) $\widetilde{u''T''}$ scaled by $(\Delta U^2 \Delta T(x/D)^{-\beta}/\delta_{99}$, (b) $\widetilde{v''T''}$ scaled by $(\Delta U^2 \Delta T(x/D)^{-\beta}/\delta_{99}$ for cylindrical film at the blowing ratio $M = 1.0$. Grey lines: multiple curves on streamwise positions between $x/D = 5$ and $x/D = 16$, Black lines: Master curve (Average of multiple gray curves). For each column from the top to bottom are the result using $\beta = 0.1, 0.5, 0.9, 1.3, 1.7, 2.0$.

loss, which is balanced by the two most prominent gain terms: pressure scrambling PHI and turbulent viscous-thermal transport contribution DT. The patterns of budget terms below the center of the potential core between $y/\delta_{99} = 0.1$ and $y/\delta_{99} = 0.5$ can be treated as a mirror image of the patterns of corresponding budget terms above the center of the potential core. The center of the potential core behaves as a mirror, making the turbulent heat flux on the upper side and lower side symmetric.

Between the wall and $y/\delta_{99} = 0.1$ of the cylindrical film, the turbulent viscous-thermal transport contribution DT is the main gain in $\widetilde{u''T''}$, and the pressure scrambling PHI is the main loss. The pair of dissipation eps and convection con exhibit extremes of opposite sign: the convection con acts as a gain, and the turbulent viscous-thermal transport contribution DT acts as a loss in the upper part of this region, but their roles switch when approaching the wall. The complexity in this region arises because turbulent heat flux is limited in the confined region in the streamwise and wall-normal directions, as discussed in the above section. At $x/D = 5$, the peaks in proximity to the wall shrink, and the structure originating from the flow mechanisms in the confined region at $x/D = 2$ disappears. Conversely, the region shown above the potential core at $x/D = 2$ expands towards the wall, with generally similar shapes of source terms and sink terms, and the magnitudes of their peaks are reduced to around half. This change occurs because the confined region has already vanished at $x/D = 5$.

At $x/D = 10$, the general shapes of budget terms of $\widetilde{u''T''}$ throughout the studied jet layer thickness, except in the near-wall region, remain. Production due to the mean velocity and mean temperature $PT1$ continues to be the major gain. The sink terms are the pressure scrambling PHI and the turbulent viscous-thermal transport contribution DT, with the latter's magnitude increased from upstream to be equally large as the magnitude of the pressure scrambling PHI at this position. The increase in the turbulent viscous-thermal transport contribution DT means the diffusion of turbulence from the upper side of the jet to around is more prominent at downstream positions. The influence of the near-wall budget peak becomes minor in terms of both the magnitude and the coverage in the wall-normal direction. This is because the jet and near-wall turbulent boundary layer become detached as the jet goes downstream at this blowing ratio.

In Fig. 19 (top row), the variations of the wall-normal component of the heat flux correlations across the jet layer downstream from the cooling hole are shown in the defect scaling. The vertical component of heat flux correlations in the fan-shaped film acts as the sink throughout the positions downstream from the hole. The peak magnitude is located at the upper side of the jets, which is similar to the pattern shown for the streamwise component of heat flux correlations at corresponding streamwise positions. The increase in the magnitude of the vertical component is uniformly distributed along the streamwise positions. For the cylindrical case, the peak located at the upper side of the jet (at around $y/\delta_{99} = 0.7 - 0.8$ with the defect scaling) maintains magnitude as the same from $x/D = 2$ to $x/D = 5$ but grows its magnitude to a most prominent extreme from $x/D = 5$ to $x/D = 10$. Apart from the peak at the upper side of the jet, a peak of the source at the lower side of the jet appears at around $y/\delta_{99} = 0.35$ when $x/D = 2$. This corresponds to the lower side of the jet. There is a local minimum between

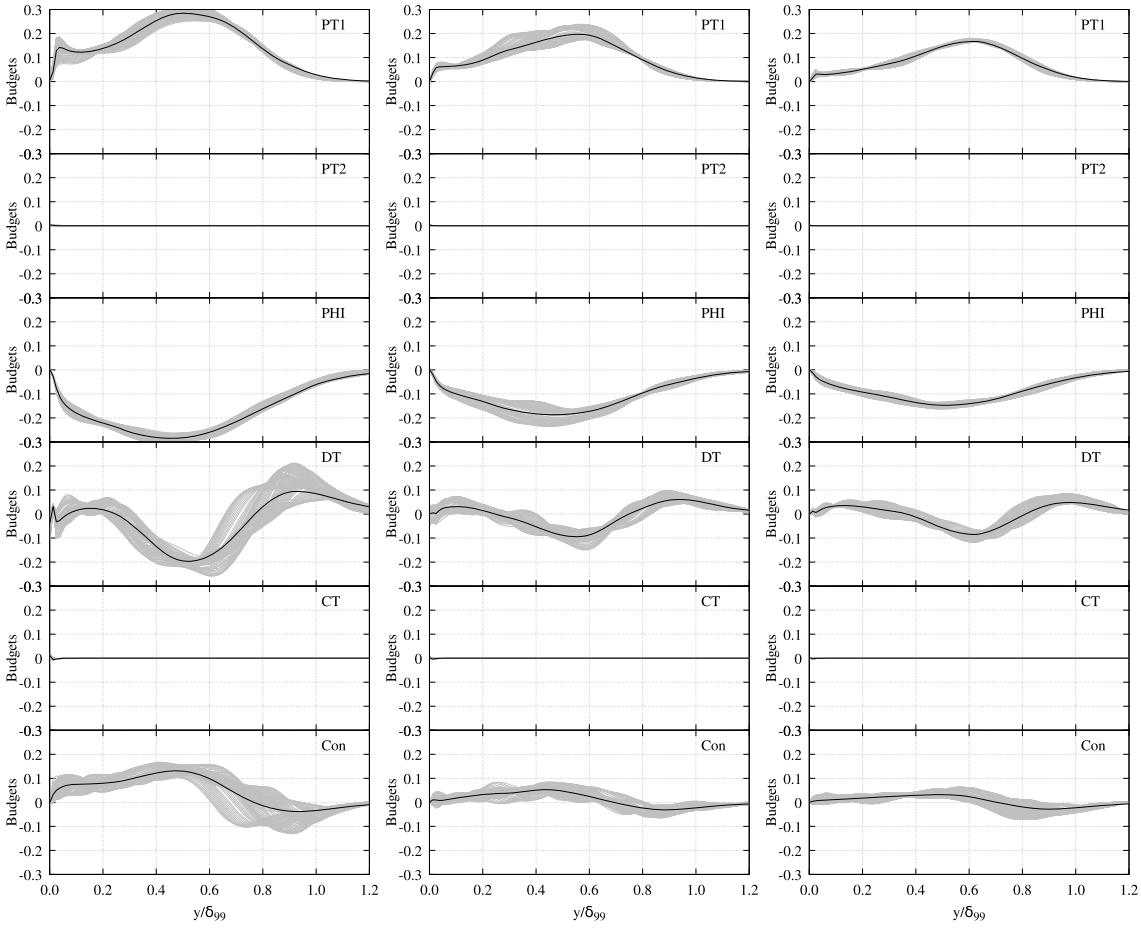

Fig. 22. Budget terms of $\widetilde{u''T''}$ scaled by $(\Delta U^2 \Delta T (x/D)^{-\beta}/\delta_{99}$ for fan-shaped film at three blowing ratios. Grey lines: multiple curves on streamwise positions between $x/D = 5$ and $x/D = 16$, Black lines: Master curve (Average of multiple gray curves). Three columns from left to right are budgets of $M = 0.5$, $M = 1.0$, $M = 1.5$. For each column from the top to bottom are corresponding production due to the mean velocity and mean temperature $PT1$, Production due to the fluctuating strain rate $PT2$, Pressure-scrambling PHI, Turbulent viscous-thermal transport contribution DT, compressibility associated terms CT, and convection Con.

$y/\delta_{99} = 0.0$ and $y/\delta_{99} = 0.2$. This corresponds to the confined region. The mechanism behind this peak and the local minimum have been described in detail, see Section 4.1.1. The potential core can be identified at $y/\delta_{99} = 0.5$ where the turbulent heat flux is shown as zero. The sign of the flux curve indicates that below the potential core heat is transferred upwards, while above the potential core the heat is transferred downwards. This can be explained as the potential core being the cold jet, and the confined region further lower than that holding the hot air entrained. Downstream from $x/D = 2$, the local minimum around $y/\delta_{99} = 0.1$ disappears because the confined region disappears. The heat in the upper side of the jet is also transferred to the jet below.

Fig. 19 (row 2-4, left column) shows the budget terms in the transport equation of wall-normal turbulent heat flux $\widetilde{v''T''}$ for the fan-shaped film at $M = 1.0$. At $x/D = 2$, the peak magnitudes of the overall budget terms are located at the extremes of the turbulent viscous-thermal transport contribution DT. At the edge of the jet ($y/\delta_{99} = 0.5$), the gain in the budgets of $\widetilde{v''T''}$ is the turbulent viscous-thermal transport contribution DT, which is balanced by the peak of production due to the mean velocity and mean temperature $PT1$, acting as the loss. In the near-wall region, the gain is the pressure scrambling PHI, balancing the negative extreme of the turbulent viscous-thermal transport contribution DT as well as production due to the mean velocity and mean temperature $PT1$ with a smaller and decreasing magnitude when going towards the wall. At $y/\delta_{99} = 0.9$, the turbulent viscous-thermal transport contribution DT behaves as the loss in $\widetilde{v''T''}$, where the pressure scrambling is the gain. An imbalance appears here due to a non-zero time gradient, which happens possibly because of the large gradient of production due to the mean velocity and the mean temperature $PT1$. When it goes downstream, the general shape of corresponding budget terms maintains the same. Compared with the patterns at $x/D = 2$, the pressure scrambling PHI grows to a more averaged distribution with the highest magnitudes of gain at below $y/\delta_{99} = 0.9$ and around $y/\delta_{99} = 0.1$, respectively, when it arrives $x/D = 10$. Also at $x/D = 10$, the production due to the mean velocity and mean temperature $PT1$ grows to a more averaged distribution, acting as the major loss from the wall to just over $y/\delta_{99} = 0.8$. From $y/\delta_{99} = 0.85$ to above, the turbulent viscous-thermal transport contribution DT becomes the major loss in $\widetilde{v''T''}$. Throughout the near-wall region and the jet region studied in this section, production due to the fluctuating strain rate $PT2$ downstream from the hole is negligible.

Fig. 19 (row 2-4, right column) shows the budget terms in the transport equation of the wall-normal turbulent heat flux $\widetilde{v''T''}$ for the cylindrical film at $M = 1.0$. At $x/D = 2$, the budget terms of $\widetilde{v''T''}$ in the jet region between $y/\delta_{99} = 0.5$ and $y/\delta_{99} = 1.2$ of the cylindrical film is similar with the structure of budget balancing in the whole jet layer of the fan-shaped film, except that the convection term becomes the gain for the cylindrical film. A lower level of magnitude is shown in this region for the cylindrical film. This means that the properties of $\widetilde{v''T''}$ budget terms above the center of the potential core in the cylindrical film correspond to the properties of $\widetilde{v''T''}$ budget terms above the wall in the

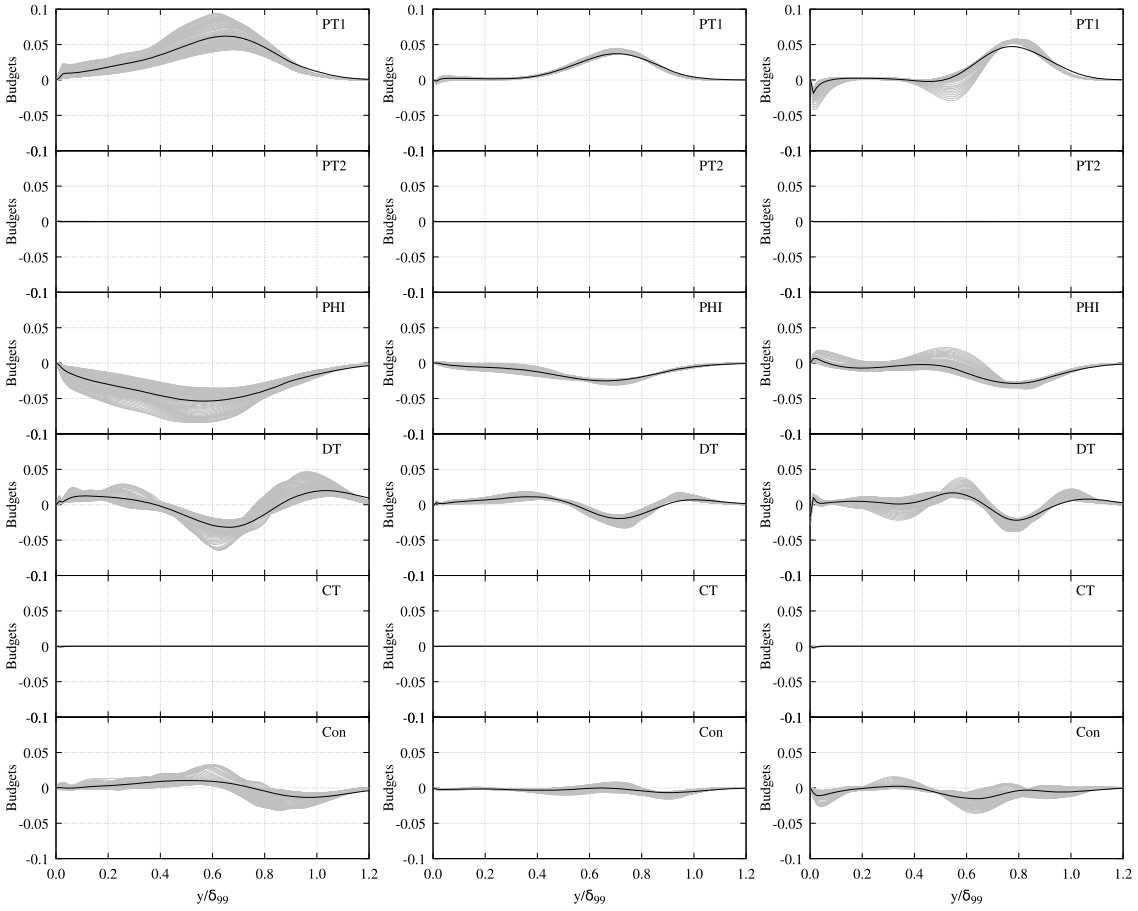

(a) $M = 0.5$ (b) $M = 1.0$ (c) $M = 1.5$

Fig. 23. Budget terms of $\widetilde{u''T''}$ scaled by $(\Delta U^2 \Delta T (x/D)^{-\beta}/\delta_{99}$ for cylindrical film at three blowing ratios. Grey lines: multiple curves on streamwise positions between $x/D = 5$ and $x/D = 15$, Black lines: Master curve (Average of multiple gray curves). Three columns from left to right are budgets of $M = 0.5$, $M = 1.0$, $M = 1.5$. For each column from the top to bottom are corresponding production due to the mean velocity and mean temperature $PT1$, Production due to the fluctuating strain rate $PT2$, Pressure-scrambling PHI, Turbulent viscous-thermal transport contribution DT, compressibility associated terms CT, and convection Con.

fan-shaped film. There are two other groups of budget peaks. One is just below the center of the potential core, which is between $y/\delta_{99} = 0.1$ and $y/\delta_{99} = 0.5$, where production due to the mean velocity and mean temperature $PT1$ is the gain and pressure scrambling PHI is the loss. This region corresponds to the lower side of the jet. The other group of high magnitude is in the proximity to the wall, with the production due to the mean velocity and mean temperature $PT1$ and unresolved dissipation acting as the gain, while pressure scrambling PHI and turbulent viscous-thermal transport contribution DT acting as the loss. The bottom of magnitude between these two groups of peak magnitude corresponds to the confined region, where the production of turbulent heat flux is low. When it goes downstream to $x/D = 5$, the pattern of both the two groups of high magnitude and the bottom shrinks to none as the confined region disappears. At $x/D = 10$, the pressure scrambling PHI becomes the major gain throughout the jet layer thickness, while production due to the mean velocity and mean temperature $PT1$ becomes the major loss throughout this region. Turbulent viscous-thermal dissipation takes the highest peak at $y/\delta_{99} = 0.7$ as the gain in $\widetilde{v''T''}$, as well as the sink at $y/\delta_{99} = 0.3$ and $y/\delta_{99} = 1.0$ as the loss. This happens because the heat is transferred from the side of the jet to around.

4.3. Universal scaling

Previous studies ([10], [9]) have identified self-similarity properties in various aspects, including wall-normal profiles, streamwise profiles of mean quantities, Reynolds stresses, and Reynolds stress budgets. These self-similarity properties enable collapsing of graphs depicting mean velocities or turbulence intensities taken at different streamwise positions when suitably rescaled. The scaling quantities employed in this process are local variables, such as the jet layer thickness, velocity defect, and temperature deficit, measured at well-defined locations within the layer. Further explanations of the velocity defect and temperature can be found in Hao and di Mare [9].

In the case of an attached flow film, the quantities of interest are located at half of the jet layer thickness. The velocity scale is defined by the velocity defect at this half-thickness point, while the temperature scale is determined by the temperature deficit at the same location. On the other hand, for a lifted flow film, the largest velocity defect and the largest temperature deficit observed in the upper part of the film are adopted as the appropriate scales for the outer region of the jet. Regarding the near-wall region, several scaling methods have been proposed for similar flow configurations. For instance, Gupta et al. (2020) demonstrated that the u_τ scaling is applicable close to the wall. However, they also showed that the buffer layer between the wall and the jet adheres to a modified law of the wall due to disruptions caused by reattachment, adverse pressure gradients, and high turbulent intensities in the upper part of the jet.

This section introduces a comprehensive external scaling approach for both the turbulent heat fluxes and their budgets, accounting for the effect of position. By employing this scaling, the budget terms obtained at locations between $x/D = 5$ and $x/D = 16$ (indicated as gray curves) collapse onto each other in Figs. 20 to 25. The budget terms are scaled

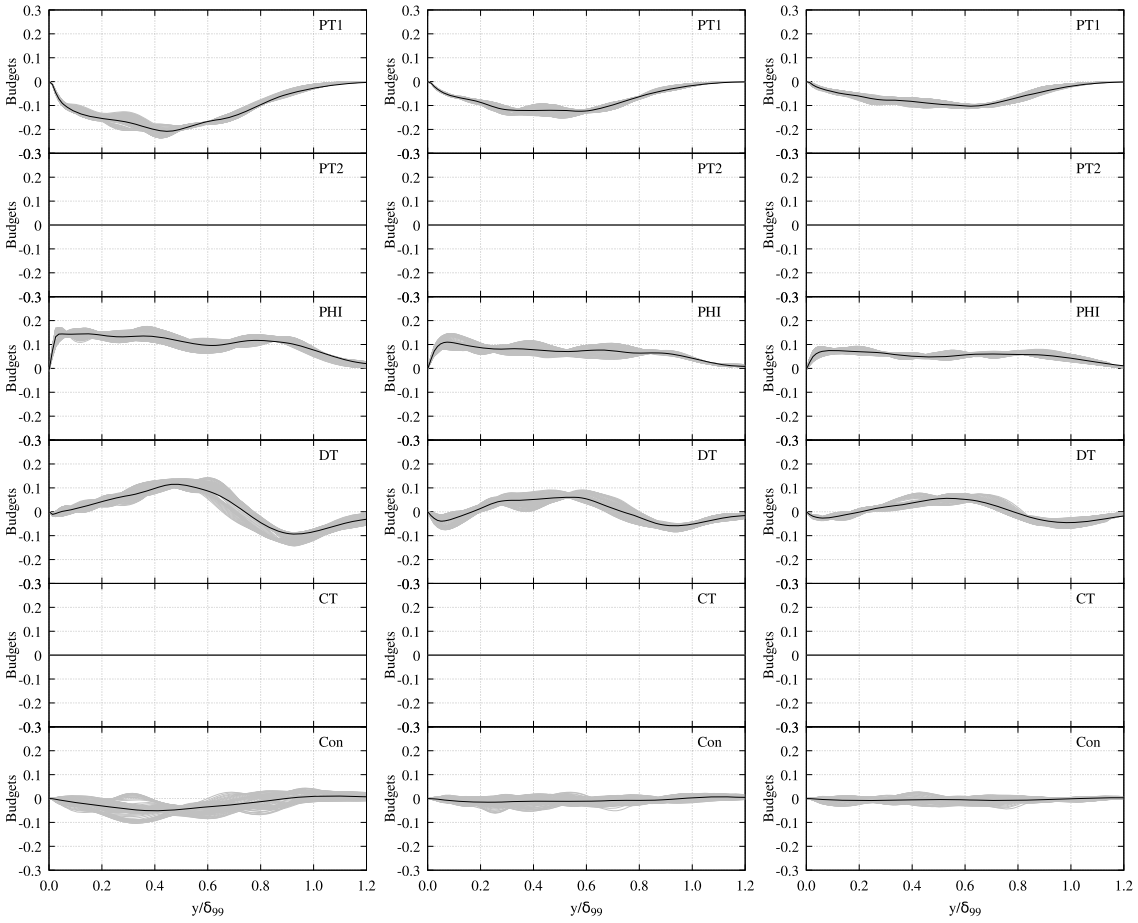

(a) $M = 0.5$ (b) $M = 1.0$ (c) $M = 1.5$

Fig. 24. Budget terms of $\widetilde{v''T''}$ scaled by $(\Delta U^2 \Delta T (x/D)^{-\beta}/\delta_{99}$ for fan-shaped film at three blowing ratios. Grey lines: multiple curves on streamwise positions between $x/D = 5$ and $x/D = 15$, Black lines: Master curve (Average of multiple gray curves). Three columns from left to right are budgets of $M = 0.5$, $M = 1.0$, $M = 1.5$. For each column from the top to bottom are corresponding production due to the mean velocity and mean temperature $PT1$, Production due to the fluctuating strain rate $PT2$, Pressure-scrambling PHI, Turbulent viscous-thermal transport contribution DT, compressibility associated terms CT, and convection Con.

using the factor $(\bar{\rho}\Delta U^2 \Delta T (x/D)^{-\beta}/\delta_{99})$, while the turbulent heat fluxes are scaled using the factor $(\bar{\rho}\Delta U \Delta T)$, as described in Section 4.2. The wall-normal distances from the wall are scaled by the boundary layer thickness δ_{99}. All quantities are evaluated on the median plane. The multiple gray curves are averaged to create the master curve (represented by the black curve) for each specific case in Figs. 20 to 25.

Furthermore, the sensitivity of the scaling parameter β to the type of cooling hole is evident. To determine the appropriate scaling factor, 30 values of β ranging from -1 to 2 are used to plot scaled turbulent heat flux budget terms along the wall-normal distribution at various streamwise slices. The ideal β value is chosen based on the extent to which these curves collapse into a narrow region, creating a master curve for each specific geometry under consideration. As illustrated in Fig. 20 and Fig. 21, a selection of different β values is shown for both types of film cooling at a blowing ratio of $M = 1.0$. Specifically, the first budget terms (the production due to the mean velocity and mean temperature) of the streamwise turbulent heat flux $\widetilde{u''T''}$ and the wall-normal turbulent heat flux $\widetilde{v''T''}$ are scaled using the factor $(\Delta U^2 \Delta T (x/D)^{-\beta}/\delta_{99})$.

In the case of the fan-shaped film (Fig. 20), as β increases from 0.5, the shadow region covered by the budget term curves widens relative to the peak of the corresponding master curve. The width of the shadow region is at a similar level along most parts of the wall-normal distance when comparing the results for $\beta = 0.1$ and $\beta = 0.5$, with $\beta = 0.5$ demonstrating an advantage over $\beta = 0.1$ above the wall-normal distance y/δ_{99}. On the other hand, for the cylindrical film (Fig. 21), the width of the shadow region covered by the budget term curves relative to the peak of the corresponding master curve collapses to be the narrowest when $\beta = 0.9$. Therefore, based on the results and the method of selecting β, $\beta = 0.5$ is chosen for the fan-shaped cooling hole, while $\beta = 0.9$ is selected for the cylindrical cooling hole.

Figs. 22-25 demonstrate the capability of the adopted scaling approach in making budget terms associated with the transport equation of turbulent heat fluxes (both streamwise and wall-normal components) collapse into narrow regions. These master curves are generated by averaging budget terms obtained from multiple streamwise positions in the wall jet far field, all at the same nondimensional distance δ_{99}. In Section 4.2, we extensively discussed the shape of these master curves, which exhibits a consistent mechanism. For each type of film cooling hole, the shape and scale of the master curves at different blowing ratios collapse, forming a single dataset. Furthermore, the analysis indicates that the amplitude of scaled turbulent heat transfer budget terms on the master curve shows little dependency on the blowing ratio, but rather relies on the non-dimensional streamwise distance from the cooling hole.

When comparing the two types of cooling holes under consideration, it is evident that the master curves of the scaled budget terms at various blowing ratios exhibit greater proximity in the fan-shaped case compared to the cylindrical case. The scaled budget terms in cylindrical film cases, notably the wall-normal components, demonstrate substantial variations due to the differing mechanisms of jet flow in such configurations: in the context of $M = 0.5$, the jet remains attached, while at $M = 1.5$, it becomes lifted off, and at $M = 1.0$, an intermediate

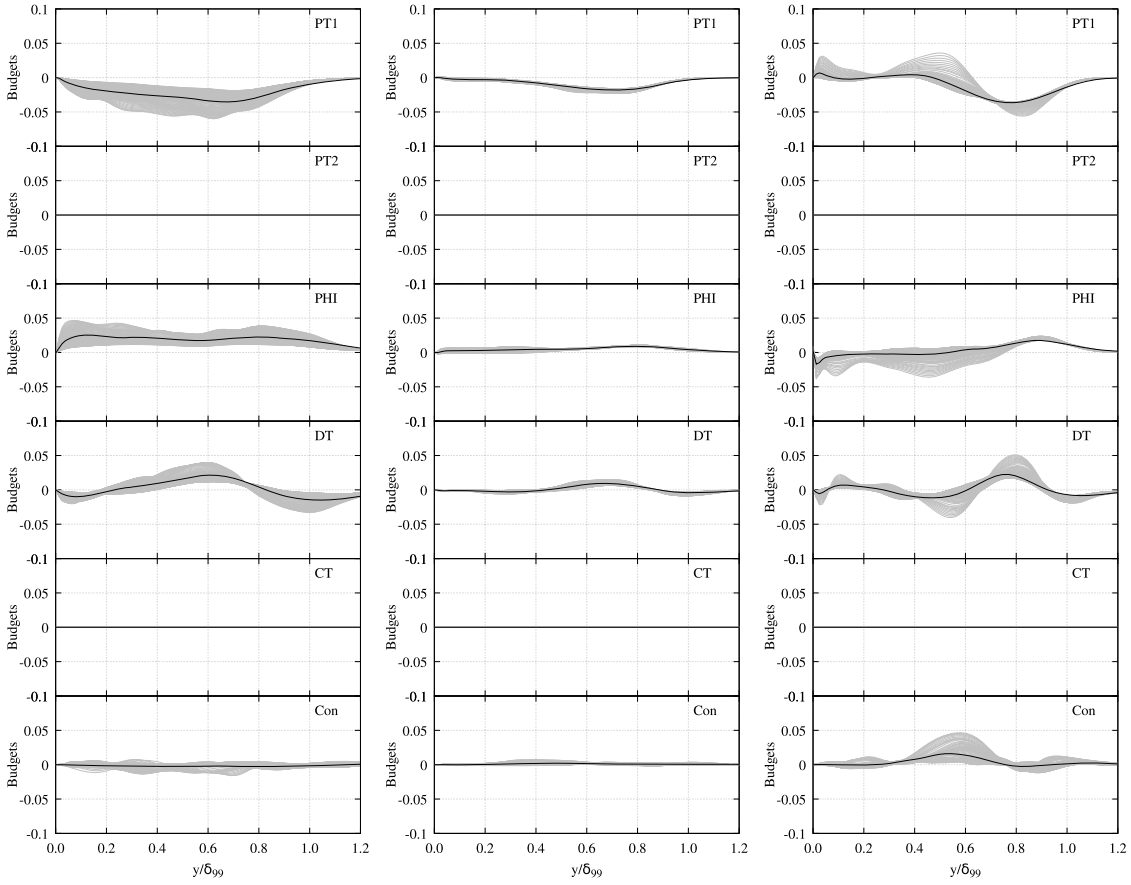

(a) $M = 0.5$ (b) $M = 1.0$ (c) $M = 1.5$

Fig. 25. Budget terms of $\widetilde{v''T''}$ scaled by $(\Delta U^2 \Delta T(x/D)^{-\beta}/\delta_{99}$ for cylindrical film at three blowing ratios. Grey lines: multiple curves on streamwise positions between $x/D = 5$ and $x/D = 15$, Black lines: Master curve (Average of multiple gray curves). Three columns from left to right are budgets of $M = 0.5$, $M = 1.0$, $M = 1.5$. For each column from the top to bottom are corresponding production due to the mean velocity and mean temperature $PT1$, Production due to the fluctuating strain rate $PT2$, Pressure-scrambling PHI, Turbulent viscous-thermal transport contribution DT, compressibility associated terms CT, and convection Con.

status is observed. It is noteworthy that heat transfers under different film cooling operating conditions, despite having different mechanisms, exhibit similar characteristics with a consistent scaling exponent β, creating a scattered distribution.

For further discussion, the turbulent heat flux in the region downstream of approximately $5D$ is relatively straightforward to model, as it exhibits self-similarity. The main challenges in achieving accurate turbulent heat flux terms arise within the first $5D$ from the film injection point. Previous RANS-based results have shown that while RANS predictions capture the correct asymptotic decay of quantities such as effectiveness, they often fail to predict the correct magnitude. The near-field downstream of the film exit is the region where deviations from self-similarity and strong three-dimensional flows occur, posing difficulties for RANS models. However, further downstream, the evolution of the coolant jet becomes less problematic due to the flow becoming self-similar. As a result, the quality of RANS predictions in terms of heat transfer is mostly determined by the near-field region, which is not favorable for the gradient diffusion model. Hence, this discovery of self-similarity offers the potential to enhance RANS predictions by utilizing the master curves of each budget component in the transport equation of the turbulent heat flux to generalize the suitable heat flux model. This can help avoid the higher computational cost associated with LES while maintaining prediction quality in the future stud of film cooling heat transfer.

5. Conclusion

A detailed study of the structure of turbulent heat fluxes and turbulent heat flux budgets has been presented for fan-shaped and cylindrical cooling films. Three scaling methods are adopted for the general view in the three-dimensional field, the property at specific downstream positions on the centerline, and the self-similarity pattern of the collapsed characteristics along continuous downstream positions, respectively. Following a gradually deeper exploration using a gradually more comprehensive scaling method, a complete defect scaling method useful for turbulent heat flux budgets has been discovered by the end of this paper.

A qualitative study of the heat transfer characteristics is first shown. For the fan-shaped cases, the Favre-averaged temperature, the variance of temperature, and turbulent heat fluxes are concentrated in a weakly curved layer, with a structure that is essentially unchanged as the jet evolves downstream. For the cylindrical film, the blowing ratio controls the structure of the jet as well as the strength of the second motion in the $z - y$ plane. At higher blowing ratios, a potential core and a confined region become visible. A qualitative summary of the structure of the film in terms of jet edge, potential core, the lower edge of the jet, and confined region is proposed. The four regions are classified based on their positions and the relative magnitudes of the mean temperature, turbulent heat fluxes, and temperature variance in each region are highlighted. The potential core is characterized by low levels of temperature variance $\widetilde{T''T''}$. The confined region is characterized by low levels of wall-normal component of the turbulent heat flux $\widetilde{v''T''}$.

A detailed examination of the turbulent heat flux budgets is then offered. It is shown that the structure of fan-shaped films stays as two layers and the budget of the $\widetilde{u''T''}$ turbulent heat fluxes is dominated by production due to mean velocity and temperature, and pressure scrambling in the jet edge. The budget of the $\widetilde{v''T''}$ is dominated by turbulent viscous-thermal transport contribution and production due to mean velocity and temperature. The production due to fluctuating strain is negligible in both geometries and at all positions examined. In cylindrical films at moderate blowing ratios, the presence of a potential core and confined region is reflected in the budgets a short distance downstream of the injection location by the apparent subdivision of the budget term profiles into a region identical to the fan shape case, and a region - closer to the wall - with essentially mirrored characteristics.

Furthermore, the self-similarity pattern has been discussed for the turbulent heat flux budgets using the final version of the scaling method. In principle, the magnitude of the budget terms varies as the film jet evolves downstream. A modified scaling law obtained from Hao and di Mare [11] is applied to the budgets of the turbulent heat fluxes, with the effect of position included as an exponential component. It is shown that the scaling law makes the magnitude of the budget terms invariant with the downstream position and highlights the universality of the shape of the budget term profiles. The existence of universal shapes for the budget terms highlights properties of self-similarity that have so far escaped clarification. Such properties indicate that the numerical prediction of the turbulent heat fluxes in film cooling flows and a large distance downstream of the films is not exceedingly problematic and that all inaccuracies are accrued in the early history of the film.

CRediT authorship contribution statement

Muting Hao: Conceptualization (equal), Data curation (equal), Investigation (equal), Methodology (equal), Software (equal), Validation (equal), Visualization (equal), Writing – original draft (equal), Writing – review & editing (equal), **Luca di Mare:** Conceptualization (equal), Funding acquisition (equal), Supervision (equal), Writing – review & editing (equal).

Declaration of competing interest

The authors have no conflicts to disclose.

Data availability

Data will be made available on request.

Acknowledgements

Rolls-Royce (grant No. DFR03150) plc is gratefully acknowledged for supporting this work and for granting permission for its publication. The authors sincerely thank Romero Eduardo, Frederic Goenaga, and Cristian Orozco Pineiro in Rolls-Royce plc for helpful discussion. The authors also acknowledge the use of the University of Oxford Advanced Research Computing (ARC) facility in carrying out this work. http://dx.doi.org/10.5281/zenodo.22558. Part of this work was also performed using resources provided by the Cambridge Service for Data Driven Discovery (CSD4) operated by the University of Cambridge Research Computing Service (www.csd3.cam.ac.uk), provided by Dell EMC and Intel using Tier-2 funding from the Engineering and Physical Sciences Research Council and Science and Technology Facilities Council (www.dirac.ac.uk) (capital grant EP/T022159/1).

References

[1] R.D.W. Bowersox, Extension of equilibrium turbulent heat flux models to high-speed shear flows, J. Fluid Mech. 633 (2009) 61–70, https://doi.org/10.1017/s0022112009007691.

[2] C. Brun, M.P. Boiarciuc, M. Haberkorn, P. Comte, Large eddy simulation of compressible channel flow, Theor. Comput. Fluid Dyn. 22 (2008) 189–212, https://doi.org/10.1007/s00162-007-0073-y.

[3] L. Duan, M.P. Martín, Direct numerical simulation of hypersonic turbulent boundary layers. Part 4. Effect of high enthalpy, J. Fluid Mech. 684 (2011) 25–59, https://doi.org/10.1017/jfm.2011.252.

[4] C.D. Ellis, Turbulent closure analysis in heated separated and reattached flow using eddy-resolving data, Phys. Fluids 32 (2020) 045115, https://doi.org/10.1063/1.5141750.

[5] C. Flageul, S. Benhamadouche, É. Lamballais, D. Laurence, DNS of turbulent channel flow with conjugate heat transfer: effect of thermal boundary conditions on the second moments and budgets, Int. J. Heat Fluid Flow 55 (2015) 34–44, https://doi.org/10.1016/j.ijheatfluidflow.2015.07.009.

[6] H. Foysi, S. Sarkar, R. Friedrich, Compressibility effects and turbulence scalings in supersonic channel flow, J. Fluid Mech. 509 (2004) 207–216, https://doi.org/10.1017/s0022112004009371.

[7] M. Gritsch, A. Schulz, S. Wittig, Adiabatic wall effectiveness measurements of film-cooling holes with expanded exits, J. Turbomach. 120 (1998) 549–556, https://doi.org/10.1115/1.2841752.

[8] M. Hao, J. Hope-collins, L. di Mare, Generation of turbulent inflow data from realistic approximations of the covariance tensor, Phys. Fluids 34 (2022) 115140, https://doi.org/10.1063/5.0106664.

[9] M. Hao, L. di Mare, Budgets of Reynolds stresses in film cooling with fan-shaped and cylindrical holes, Phys. Fluids 35 (2023) 086103, https://doi.org/10.1063/5.0140670.

[10] M. Hao, L. di Mare, Reynolds stresses and turbulent heat fluxes in fan-shaped and cylindrical film cooling holes, Int. J. Heat Mass Transf. 214 (2023) 124324, https://doi.org/10.1016/j.ijheatmasstransfer.2023.124324.

[11] M. Hao, L. di Mare, Scaling and similarity laws in three-dimensional wall jets, Phys. Fluids 35 (2023) 075102, https://doi.org/10.1063/5.0140671.

[12] M. Hao, F. Wang, J. Hope-Collins, M.E. Rife, L. di Mare, Template-based hexahedral mesh generation for turbine cooling geometries, in: Turbomachinery, vol. 2C, American Society of Mechanical Engineers, 2020, https://doi.org/10.1115/gt2020-14660.

[13] J. Huang, G.L. Nicholson, L. Duan, M.M. Choudhari, R.D. Bowersox, Simulation and modeling of cold-wall hypersonic turbulent boundary layers on flat plate, in: AIAA Scitech 2020 Forum, American Institute of Aeronautics and Astronautics, 2020, https://doi.org/10.2514/6.2020-0571.

[14] P.G. Huang, G.N. Coleman, P. Bradshaw, Compressible turbulent channel flows: DNS results and modelling, J. Fluid Mech. 305 (1995) 185–218, https://doi.org/10.1017/s0022112095004599.

[15] T. Kawata, T. Tsukahara, Spectral analysis on transport budgets of turbulent heat fluxes in plane Couette turbulence, Energies 15 (2022) 5258, https://doi.org/10.3390/en15145258.

[16] T. Miura, K. Matsubara, A. Sakurai, Turbulent-heat-flux and temperature-variance budgets in a single-rib mounting channel, J. Therm. Sci. Technol. 7 (2012) 120–134, https://doi.org/10.1299/jtst.7.120.

[17] M.V. Morkovin, Effects of compressibility on turbulent flows, Méc. Turbul. 367 (1962) 26.

[18] F. Muldoon, S. Acharya, Analysis of k and epsilon budgets for film cooling using direct numerical simulation, AIAA J. 44 (2006) 3010–3021, https://doi.org/10.2514/1.20597.

[19] G. Nicholson, J. Huang, L. Duan, M.M. Choudhari, Simulation and modeling of hypersonic turbulent boundary layers subject to adverse pressure gradients due to streamline curvature, in: AIAA AVIATION 2021 FORUM, American Institute of Aeronautics and Astronautics, 2021, https://doi.org/10.2514/6.2021-2891.

[20] G.L. Nicholson, J. Huang, L. Duan, M.M. Choudhari, B. Morreale, R.D. Bowersox, Budgets of Reynolds stresses and turbulent heat flux for hypersonic turbulent boundary layers subject to pressure gradients, in: AIAA SCITECH 2022 Forum, American Institute of Aeronautics and Astronautics, 2022, https://doi.org/10.2514/6.2022-1059.

[21] C.L. Ribault, R. Friedrich, Investigation of transport equations for turbulent heat fluxes in compressible flows, Int. J. Heat Mass Transf. 40 (1997) 2721–2738, https://doi.org/10.1016/s0017-9310(96)00213-x.

[22] P. Schlatter, R. Örlü, Q. Li, G. Brethouwer, J.H.M. Fransson, A.V. Johansson, P.H. Alfredsson, D.S. Henningson, Turbulent boundary layers up to re $\theta = 2500$ studied through simulation and experiment, Phys. Fluids 21 (2009) 051702, https://doi.org/10.1063/1.3139294.

[23] M. Shadloo, A. Hadjadj, F. Hussain, Statistical behavior of supersonic turbulent boundary layers with heat transfer at $ma_{\inf} = 2$, Int. J. Heat Fluid Flow 53 (2015) 113–134, https://doi.org/10.1016/j.ijheatfluidflow.2015.02.004.

[24] M.S. Shadloo, A. Hadjadj, F. Hussain, Temperature-invariant scaling for compressible turbulent boundary layers with wall heat transfer, Heat Transf. Eng. 39 (2017) 923–932, https://doi.org/10.1080/01457632.2017.1357675.

[25] M. Shahab, G. Lehnasch, T. Gatski, P. Comte, Statistical characteristics of an isothermal, supersonic developing boundary layer flow from dns data, Flow Turbul. Combust. 86 (2011) 369–397.

[26] K. Thole, M. Gritsch, A. Schulz, S. Wittig, Flowfield measurements for film-cooling holes with expanded exits, J. Turbomach. 120 (1998) 327–336, https://doi.org/10.1115/1.2841410.

[27] K.W. Thompson, Time dependent boundary conditions for hyperbolic systems, J. Comput. Phys. 68 (1987) 1–24.
[28] M.A. Vyas, D.A. Yoder, D.V. Gaitonde, Reynolds-stress budgets in an impinging shock-wave/boundary-layer interaction, AIAA J. 57 (2019) 4698–4714, https://doi.org/10.2514/1.j058487.
[29] Y.S. Zhang, W.T. Bi, F. Hussain, X.L. Li, Z.S. She, Mach-number-invariant mean-velocity profile of compressible turbulent boundary layers, Phys. Rev. Lett. 109 (2012), https://doi.org/10.1103/physrevlett.109.054502.